BILINGUAL PUBLISHING CO.
Pioneer of Global Academics Since 1984

01

Journal of Mechanical Engineering Research

Volume 3 | Issue 1 | March 2020 | ISSN 2630-4945 (Online)

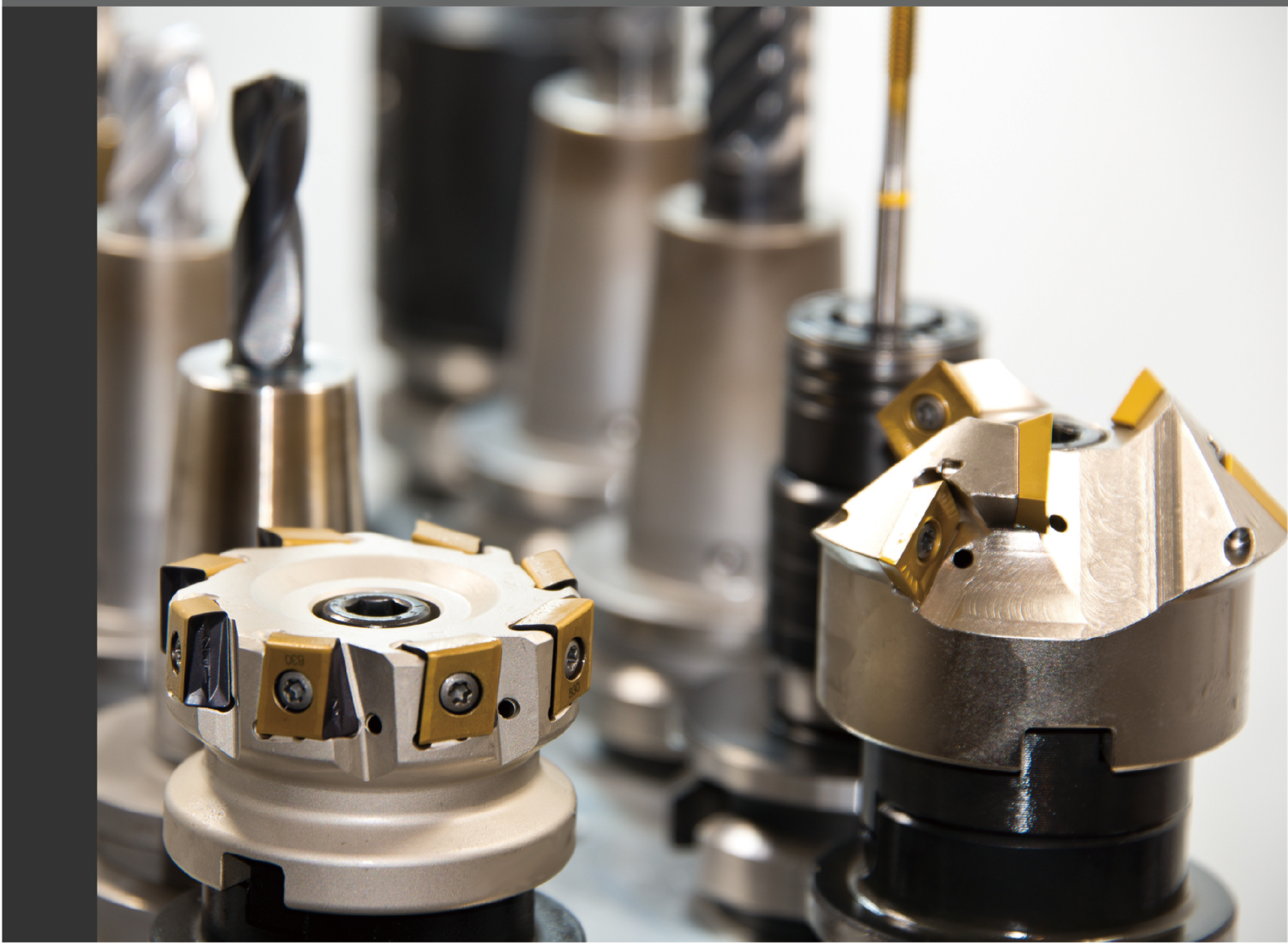

APSCI creative commons CNKI中国知网 www.cnki.net 中国知识基础设施工程 Google scholar Crossref MyScienceWork

BILINGUAL PUBLISHING CO.
Pioneer of Global Academics Since 1984

Volume 3 Issue 1 • March 2020 • ISSN 2630-4945 (Online)

Journal of Mechanical Engineering Research

BILINGUAL PUBLISHING CO.

Pioneer of Global Academics Since 1984

BILINGUAL PUBLISHING CO.
Pioneer of Global Academics Since 1984

Volume 3 | Issue 1 | March 2020 | Page 1-29
Journal of Mechanical Engineering Research

Contents

Article

BILINGUAL PUBLISHING CO.
Pioneer of Global Academics Since 1984

Journal of Mechanical Engineering Research
http://ojs.bilpublishing.com/index.php/jmer

ARTICLE

Numerical Investigation on Heat Transfer Enhancement Inside a Rectangular Microchannel with Vortex Generator using TiO_2, Cuo-water Nanofluids

Arash Behaeen* **Mohammad Nimafar**

Department of Mechanical Engineering, Central Tehran Branch, Islamic Azad University, Tehran, Iran

ARTICLE INFO

Article history
Received: 16 December 2019
Accepted: 17 January 2020
Published Online: 31 March 2020

Keywords:
Average heat transfer coefficient
Longitudinal vortex generator
Microchannel
Nanofluid

ABSTRACT

One of the innovative ways to improve heat transfer properties of heat exchangers, is using nanofluids instead of traditional fluids. Due to presence of metal and oxides of metal particles in nanofluids structure, they have better potential in different environments and conditions than conventional fluids and having higher thermal conductivity causes improvements in heat transfer properties. In this research flow of two different nanofluids through a rectangular microchannel containing a different number of longitudinal vortex generators (lvgs), has been investigated. Simulations conducted under laminar flow boundary condition and for varied Reynolds numbers of 100 to 250. Considered volumetric concentration in this paper is 1, 1/6 and 2/3 %. Results showed, nanofluids and the LVGs notably improve the heat transfer rates within the microchannel. havg improved with increasing the nanoparticles volume concentrations and Reynolds number, while the opposite trends recognized for pressure drop. havg improved for 4 to 12 and 9 to 18% for TiO_2 and CuO nanofluids, respectively for different volume concentrations in simple microchannel. For lvg-enhanced microchannel the amount of improvements is about 9-14 and 5-10% for CuO and TiO_2, respectively. Also using vortex generators alone improved havg for 15-25% for different number of lvgs.

1. Survey

Heat exchangers are a significant part of numerous industrial uses and liable for heat transfer within fluids. Their utilizations involve air conditioning systems, gas turbine coolers, etc. Using of microchannel heat exchangers and nanofluids as an operating fluid has attracted many researchers to improve heat transfer performance in recent years. According to these subjects:

Toh et al. [1] examined heat transfer happenings and fluid flow within a microchannel under constant heat flux; it was noticed that heat inputs decrease the frictional disadvantages, especially at lower Re. Heris et al. [2] experimentally studied the forced flow of Al_2O_3/water inside a tube. The convection heat transfer of nanofluid analyzed. The tube considered to be circular, and the laminar boundary condition was applied for fluid. Outcomes indicated the improvement of heat transfer via the presence of the nanoparticles in the fluid. Bianco et al. [3] investigated nanofluid forced convection in circu-

**Corresponding Author:*
Arash Behaeen,
Department of Mechanical Engineering, Central Tehran Branch, Islamic Azad University, Tehran, Iran;
Email: arash.behaeen@gmail.com

 DOI: https://doi.org/10.30564/jmer.v3i1.1568

lar tubes numerically. Results showed that heat transfer enhances with particle volume concentration, but is followed by growing wall shear stress states. he et al. [4] studied the convective heat transfer of TiO_2 nanofluids inside a vertical tube. effects of nanoparticles concentrations, Re, and numerous nanoparticles aggregates sizes investigated. Duangthongsuk and Wongwises [5] experimentally examined the heat transfer performance and pressure drop of TiO_2-water nanofluids. turbulent regime boundary condition applied inside a flat double tube counter-flow heat exchanger. Results revealed that the heat transfer coefficient rose when using nanofluid instead of conventional fluid and improved with raising the Re and particle concentrations. Demir et al. [6] studied the forced convection flow within a horizontal tube numerically. constant wall temperature condition was applied, and simulations conducted for two different nanofluids. outcomes proved the heat transfer improvement due to the bearing of nanoparticles in the fluid. Kalteh et al. [7] investigated nanofluid forced convection within a wide microchannel heat sink. both numerical and experimental analyses were conducted. For the numerical part of this study, a two-phase Eulerian-Eulerian method using the finite volume approach adopted. Result showed better agreement between experimental and the two-phase method compared to homogeneous modeling. Lotfi et al. [8] experimentally analyzed heat transfer improvement of MWNT-water nanofluid within a heat exchanger. a shell and tube heat exchanger was used in this paper. Carbon nanotubes manufactured by the use of catalytic chemical vapor deposition (CCVD) method over Co-Mo/MgO nanocatalyst. Outcomes indicated that heat transfer improves when using multi-walled nanotubes instead of conventional fluid. Fazeli et al. [9] investigated the heat transfer properties of a small heat sink, which uses SiO_2-water nanofluids as coolant numerically and experimentally. Experimental outcomes revealed that scattering SiO_2 nanoparticles in water improve the overall heat transfer coefficient remarkably while thermal immunity of heat sink decreases up to 10%. Nimafar et al. [10] experimentally investigated the mixing process of three different passive micromixers and presented a new type of micromixers called the H micromixers. in another study Nimafar et al. [11] investigated separation and recombination micromixer in confronting with basic T and O type micromixers experimentally. Kabeel et al. [12] studied the impacts of using nanoparticles on corrugated plate heat exchanger performance. An experimental test loop has formed to study the PHE thermal properties such as heat transfer coefficient and pressure

Nomenclature			
		subscripts	
C	Correction coefficient	μ	Dynamic viscosity(kg/m.s)
C_p	Specific heat(j/kg.k)	φ	Particle volume concentration
C_d	Drag coefficient	ht	Heated zone
D_h	Hydraulic diameter(m)	nf	nanofluid
dlvg	Diameter of longitudinal vortex generators	p	Nanoparticle
N	Normal vector of surface		
Nu	Nusselt number		
P	Pressure(pa)		
Pr	Prandtl number		
F	Fanning friction factor		
G	Gravity(m/s2)		
H	Heat transfer coefficient(w/m2.k)		
K	Thermal conductivity(w/m.k)		
L	Length(m)		
q"	Heat flux(w/m2)		
Re	Reynolds number		
T	Time(s)		
T	Temperature(K)		
υ	Velocity vector(m/s)		
X	Distance from the heated zone inlet		
V	Volume(m3)		

DOI: https://doi.org/10.30564/jmer.v3i1.1568

drop for various concentrated volume fractions of Al_2O_3 nanoparticles. Shkarah et al. [13] studied heat transfer in a microchannel heat sink. graphene, aluminum, and silicon substrates used for this study. Results from this numerical study showed that graphene most effectively reduced the thermal resistance. Viktorov and Nimafar [14] presented a new generation of 3D splitting and recombination (SAR) passive micromixer with microstructures placed on the top, and bottom floors of microchannels called a chain mixer. to analyze the flow structure of this type of passive micromixer, the mixing performance and pressure drop of the microchannel both experimental and numerical methods conducted. Wael aly [15] performed a CFD research to analyze the heat transfer and pressure drop characteristics of water-based Al_2O_3 nanofluid inside coiled tubes in tube heat exchangers. Results presented various behavior depending on the parameter selected for the comparison with the base fluid. Furthermore, analyzing at the same Reynolds or Dn showed the heat transfer coefficient improvements by raising the coil diameter and nanoparticle volume concentration. Bianco et al. [16] analyzed the turbulent convection of Al_2O_3-water nanofluid inside a round tube numerically employing a mixture model. Zhang et al. [17] experimentally studied TiO_2-water nanofluid single-phase flow and heat transfer features in a multiport channel flat tube. Results showed that friction factor and Nu of the nanofluids were higher than water, and both nanofluid's density and particle migration notably influenced the friction factor. Tiwari et al. [18] investigated heat transfer and fluid stream of CeO_2 and Al_2O_3 nanofluids inside corrugated chevron plates, plate heat exchanger as a homogeneous mixture numerically. CFD simulations showed that the corrugation design of the plate amplifies turbulence and vortices of fluid, which results in great heat transfer rates. Sarafraz and Hormozi [19] investigated the heat transfer and pressure drop properties of multi-walled carbon nanotube (MWCNT) aqueous nanofluids within a plate heat exchanger experimentally. Results showed that the heat transfer coefficient could enhance by increasing the flow rate and concentration of nanoparticles. Khajeh arzani et al. [20] investigated thermophysical characteristics, heat transfer and pressure drop of covalent and noncovalent functionalized graphene nanoplatelet based water nanofluids in a terete heat exchanger, experimentally, and numerically. Xia et al. [21] studied the properties of fluid flow and mass transfer in a new micromixer with rifts and baffles. both numerical and experimental methods used to validate the results. The impacts of rifts and baffles examined, considering both mixing performance and pressure drop at different Re. Sakanova et al. [22] investigated the curved channel formation and usage of nanofluids. Results showed that in case of using pure water as the coolant, the heat transfer performance of the channel notably improves compared with a conventional straight channel, while replacement of the pure water by nanofluids, made the effects of curved wall unnoticeable. Behrangzade and Heyhat [23] studied influences and potential of using dispersed nano-silver nanofluid with water as the base fluid inside a plate heat exchanger experimentally. Results showed significant improvements in the overall heat transfer coefficient, but pressure drop growth was not significant. Zarringhalam et al. [24] investigated the flow of CuO nanofluid experimentally. The influences of the Reynolds number and volume fraction on the heat transfer coefficient and pressure drop examined in this article. Like other studies, outcomes showed that heat transfer coefficient rises during using nanofluid instead of conventional fluids. It was observed that heat transfer coefficient and Nu increases with raising the substantial volume fraction and Re. Although the increase rate was lower at higher Reynolds numbers. Ebrahimnia-bajestan et al. [25] studied the effects of using TiO_2-water nanofluid as operating fluid inside heat exchangers in solar systems. Both experimental and numerical methods used to validate the results. Results from both experimental and numerical procedures showed that the heat transfer coefficient rises with an increase in volume concentration and Re. Chen et al. [26] studied micromixers with serpentine microchannels and analyzed their mixing performance experimentally and numerically.

Square-wave, multi-wave, and zigzag structures were picked for study. Results from both numerical and experimental results showed that square wave serpentine micromixers are more efficient and flexible than the other two structures. Sheikholeslami and Nimafar [27] analyzed hydrothermal behavior of CuO water-based nanofluid inside a complex-shaped cavity. Impacts of different parameters such as Ra, volume fraction, and the number of undulations investigated and the homogenous model used to simulate nanofluid. Fsadni et al. [28] studied the turbulent flow of Al_2O_3 nanofluid through a helically coiled rectangular-circular tube heat exchanger numerically. The heat exchanger was under constant wall heat flux, and the heat transfer and pressure drop features of this heat exchanger investigated under different conditions. Zhang et al. [29] used micro fin structure and nanofluid to enhance heat transfer performance of a microchannel. They studied heat transfer and pressure drop inside the microchannel, experimentally. Outcomes revealed that with increasing the number of fins, Nu and friction factor increases. It was found that micro fin and

 DOI: https://doi.org/10.30564/jmer.v3i1.1568

nanofluid techniques are both efficient ways to improve the heat transfer performance of microchannel. Rao et al. [30] studied Al_2O_3 nanofluid forced convective heat transfer coefficient under turbulent flow boundary condition inside a single pass, multi-tube, counterflow shell and tube heat exchanger. Results revealed higher forced convection than water flow at the same conditions. Diao et al. [31] investigated the heat transfer and flow of MWCNT-water nanofluid inside a multiport microchannel with smooth and micro fin structure using experimental methods. Results showed that the heat transfer is higher in the micro fin tubes compared with smooth surface, but the heat transfer enhancement was lower in micro fin tube. Baheri islami et al. [32] studied the mixing performance of non-newtonian nanofluids inside micromixers numerically using the mixture model. They found out that the number of injection flows and baffles can be very efficient in mixing performance. Sheikholeslami and Nimafar [33] studied nanofluid flow and heat transfer within two circular cylinders in the presence of a magnetic field. Multiple active parameters such as aspect ratio, Eckert number, Reynolds number and Hartmann number had examined. They found out that the temperature gradient develops with increasing Ha and Ec, and reduces with increasing Re. in another article [34] they reported the influences of melting heat transfer on nanofluid flowing, in the presence of Lorentz forces. Different shapes of nanoparticles considered. Results showed that the maximum Nusselt number occurs at platelet shape, and the temperature reduces with an increase in melting parameters.

In this research, flow and heat transfer performance of TiO_2-water and CuO-water nanofluids through a longitudinal rectangular microchannel using vortex generators inside investigated numerically. Results reported for different effective parameters such as Re, volume concentration, and the number of vortex generators (lvgs). Variations of heat transfer coefficient, Nu, and pressure drop reported using a single-phase model by simulating the flow with ANSYS-FLUENT software.

2. Problem Description and Mathematical Model

The conferred issue is a four-sided longitudinal microchannel to investigate the effects of using longitudinal vortex generators (lvgs) and nanofluids (TiO_2 and CuO) on heat transfer performance inside this microchannel. In order to do that, at first, a comparative simulation performed between the single-phase and two-phase models at similar conditions to evaluate the difference between results of these two models. Then the rest of simulations done under presented conditions and by using single-phase model using ANSYS-FLUENT software.

In this paper, the Cartesian coordinate system used to describe the flow of the fluid, which in this coordinate, the z-axis represents streamwise direction.

The geometry of the considered issue demonstrated in figure 1. also geometrical parameters used to define the geometry of the microchannel and the vortex generators presented in table 1.

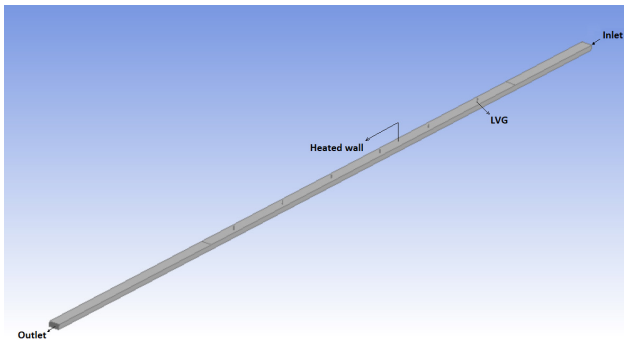

Figure 1. 3D view of investigated geometry

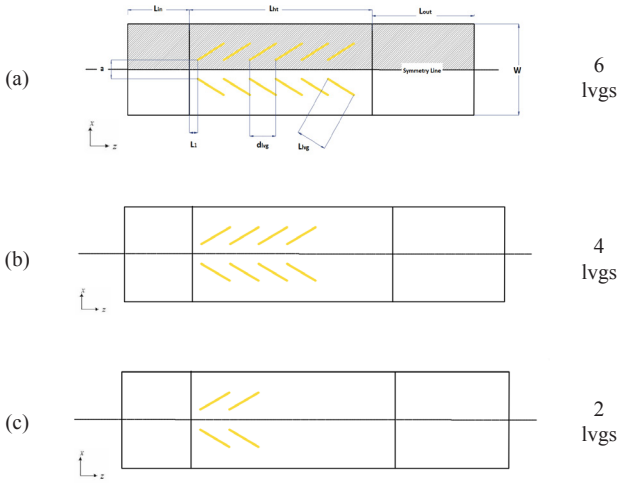

Figure 2. schematic of investigated geometry

Computational domain is divided into three zones:

(1) the inlet area with length of L_{in}, which assumed to be adiabatic and indicates the flow developing zone.

(2) the heated area, which is under constant heat flux and the vortex generators are located in this area.

(3) the outlet area, which eliminates affecting of any backflow on the final results.

Because of symmetric layout of the microchannel and to reduce the computational time and cost, only the schemed area in figure 2 (a) is considered for numerical investigation.

DOI: https://doi.org/10.30564/jmer.v3i1.1568

Table 1. Geometrical parameters of the microchannel and vortex generators

Geometric parameter	amount	Geometric parameter	amount
L_{in}	2500 µm	L1	1000 µm
L_{ht}	10^4 µm	dlvg	1600 µm
L_{out}	5000 µm	Wlvg	10 µm
W	400 µm	Llvg	140 µm
H	100µm	a	80 µm
dh	160 µm	β	30

Microchannel and vortex generators in this paper are made of silicon plates and flow of water and CuO and TiO_2 nanofluids investigated inside this microchannel as coolant. Thermophysical properties of these material presented in table 2.

Table 2. Thermophysical characteristics of materials

	K (w/m.k)	Cp (j/kg.k)	ρ (kg/m3)	µ (Pa.s)
Pure water	$-7/843*10^{-6}+0/0062R-0/54$	$6719/637-20/86T+0/0552T^2-0/0000462T^3$	$816/781+1/505T-0/003T2$	$0/00002414*10^{247/8/(t-140)}$
TiO2	8/4	710	4157	
CuO	76/5	536/6	6350	
silicon	290-0.4T	390+0.9T	2330	

Some of the other assumptions that considered in this paper are as follow:

(1) surface roughness considered zero for microchannel walls and lvgs.

(2) flow considered steady, Newtonian and laminar because of low velocities of fluid and small dimension of vortex generators.

(3) radiative heat transfer, compressibility and the effects of body forces are neglected.

Fluid flow investigated for 100, 150, 200 and 250 Reynolds numbers and for 3 different volume concentration of 1, 1/6 and 2/3 percent, inside flat microchannel and microchannel with 2, 4 and 6 pairs of vortex generators. The inlet temperature fixed at 298k and the pressure outlet condition considered for outlet. Top wall is under constant heat flux of 20 w/cm^3 and considered the heated zone of the microchannel. Non-slip and adiabatic conditions assumed for other surfaces of the microchannel.

To compare results achieved from single-phase and two-phase model, an Eulerian method assumed for each phase of nanofluid (base fluid and nanoparticles) and equations solved separately using the Eulerian-Eulerian model. Continuity, momentum and energy equations derived from ANSYS-FLUENT software [35] are as follow:

$$Vi=\int \varphi_i dV \tag{1}$$

In this equation is volume of phase i. and the relation between volume concentrations of both phases described with next equation:

$$\varphi_f+\varphi_p=1 \tag{2}$$

Continuity and momentum equations are as follow:

$$\nabla.\left(\varphi_i\ \rho_i\ \vec{\vartheta}_i\right)=0 \tag{3}$$

$$\nabla.\left(\varphi_f\rho_f\overrightarrow{\vartheta_f}\overrightarrow{\vartheta_f}\right)=-\varphi_f\nabla p+\nabla.\overline{\overline{\tau_f}}+\overrightarrow{R_{pf}} \tag{4}$$

$$\nabla.\left(\varphi_p\rho_p\overrightarrow{\vartheta_p}\overrightarrow{\vartheta_p}\right)=-\varphi_p\nabla p+\nabla.\overline{\overline{\tau_p}}+\overrightarrow{R_{pf}} \tag{5}$$

Which momentum equation is written for each phase separately in equation (4) and (5) in which in these equations is the i_{th} phase stress strain tensor that defined by equation (6) and is the interaction force between two phases of nanofluid.

$$\overline{\overline{\tau_i}}=\mu_i\nabla\overrightarrow{\vartheta_i} \tag{6}$$

$$\overrightarrow{R_{pf}}=K_{pf}(\overrightarrow{\vartheta_p}-\overrightarrow{\vartheta_f}) \tag{7}$$

K_{pf} in equation (7) is the interphase momentum exchange coefficient:

$$K_{pf}=(\varphi_f\,\varphi_p\,\rho_p\,C_D\,Re_p)/(24\tau_p) \tag{8}$$

τ_p and C_D in equation (8) are the particulate relaxation time and drag coefficient, respectively which described by:

$$\tau_p=\rho_p d_p^2/18\mu_f \tag{9}$$

$$C_D \tag{10}$$

$$=\begin{cases}\dfrac{24\left(1+0.15Re_p^{0.687}\right)}{Re_p} & ,\quad Re\le 1000\\ 0.44 & ,\quad Re>1000\end{cases}$$

(Schiller-Naumann model)

Re_p, in equation (10) is the relative Re and written as follows:

$$Re_p=\frac{\rho_f|\overrightarrow{\vartheta_p}-\overrightarrow{\vartheta_f}|d_p}{\mu_f} \tag{11}$$

In order to apply energy equation in Eulerian-Eulerian model, enthalpy equation should written for each phase separately:

$$\nabla.\left(\varphi_f\rho_f h_f\overrightarrow{\vartheta_f}\right)=\overline{\overline{\tau_f}}:\nabla\overrightarrow{\vartheta_f}-\nabla.\overrightarrow{q_f}+Q_{pf} \tag{12}$$

$$\nabla.\left(\varphi_p\rho_p h_p\overrightarrow{\vartheta_p}\right)=\overline{\overline{\tau_p}}:\nabla\overrightarrow{\vartheta_p}-\nabla.\overrightarrow{q_p}+Q_{pf} \tag{13}$$

DOI: https://doi.org/10.30564/jmer.v3i1.1568

In these equations, and are heat flux and specific enthalpy of phase i, respectively and or the heat exchanger intensity of two phases described with equation (14) as follows:

$$Q_{pf}=h_V\,(T_f-T_p) \tag{14}$$

h_V, or the volumetric heat transfer coefficient described with the next equation:

$$h_V = C \times \frac{(6k_f\varphi_p\varphi_f Nu_p)}{d_p^2} \tag{15}$$

$$C = (|5.505 - 9.606 \times 10^{-6} Re_e^2 + 1.539 \times 10^{-2} Re - 3.073 \times 10^2 \varphi|) \times 10^{-9} \tag{16}$$

C in equation (16) is a correction coefficient factor which Ebrahimnia et al[25] proposed to improve the accuracy of the Eulerian-Eulerian model. Also in equation (15), Nu_p is the nanoparticle nusselt number which describes with Ranz-Marshall correlation[36] as follows:

$$Nu_p = 2 + 0.6 Re_p^{0.5} Pr_f^{1/3} \tag{17}$$

$$Pr_f = \frac{C_{p,f}\mu_f}{k_f} \tag{18}$$

Pr_f, is the base fluid prandtl number.

3. Numerical Procedure

To estimate the heat transfer performance and fluid flow inside described rectangular microchannel with vortex generators, a single-phase model used to simulate the flow inside ANSYS-FLUENT software. To calculate the corresponding gradians, such as u, υ, w and T, a non-uniform tetrahedron structure (Figure 2) used to define and solve the computational domain. The SIMPLEC algorithm applied to model pressure-velocity coupling and the convergence criterion for this problem considered 10^{-6}, which this value is 10^{-8} for the energy equation.

Some of the important parameters of the microchannel defined as follows:

$$Re = \frac{\rho_{in}\vartheta_{in}D_h}{\mu_{in}} \tag{19}$$

$$Nu = \frac{hD_h}{k} \tag{20}$$

$$D_h = \frac{2WH}{W+H} \tag{21}$$

$$h = \frac{q''}{T_{wall,avg} - (T_{in} + T_{out})/2} \tag{22}$$

$$\Delta p = (\overline{p_{in}} - \overline{p_{out}}) \tag{23}$$

In these equations, Re is the Reynolds number, D_h is the hydraulic diameter of the microchannel, Nu and h are the Nusselt number and heat transfer coefficient, respectively and Δp is pressure drop inside microchannel.

4. Validation and Grid Independency

In order to find the least computationally expensive mesh structure, a few number of networks with different cell numbers used. In this paper, the grid independence test has done under Reynolds number of 250 while pure water flows inside the microchannel as coolant. Figure 4 represents the results gained for various mesh sizes and their diversity. Considering the difference between the results are less than 1 percent for structures with 1/8 million cells, then the mesh size of 2 million cells seemed to be suitable for all the other simulations performed in this study.

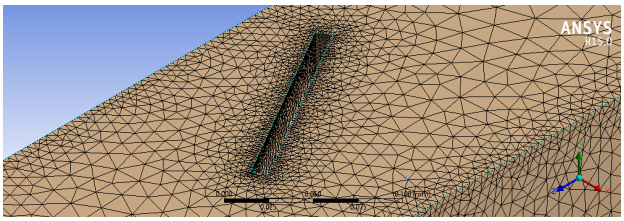

Figure 3. 3d view of mesh network

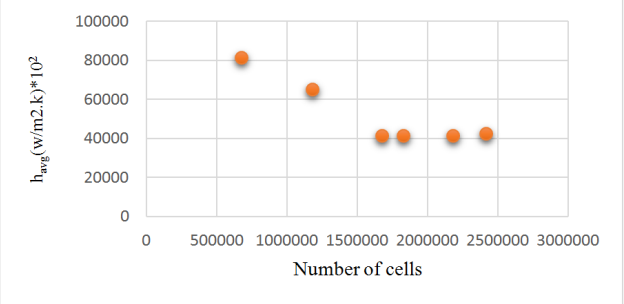

Figure 4. Grid independency test

To verify the obtained outcomes from the presented numerical method, the experimental data from Ebrahimnia et al. [25] for TiO2-water nanofluid is used. Figure 5 represents the comparison between the results of this study and the results of Ebrahimnia et al. [25]. As presented in Figure 5, the deviation between results of this paper and experimental data is about 5 to 7 %, which is acceptable. These negligible differences can be because of several factors such as simplification of physical models, using of single-phase model instead of two-phase model, experimental measurements and non-uniformity of nanoparticle sizes.

DOI: https://doi.org/10.30564/jmer.v3i1.1568

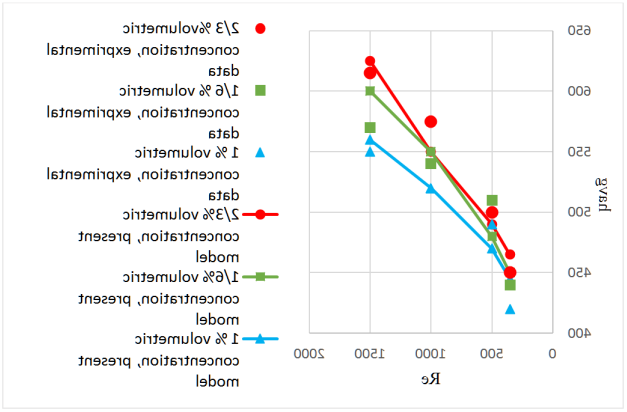

Figure 5. Validation

5. Result and discussions

In this paper, results provided for different parameters such as, convective heat transfer coefficient, Nu and pressure drop. The mentioned parameters are demonstrated as functions of Re, nanoparticle volume concentration and number of lvgs used in the microchannel.

The first figure as was promised, presented the comparison between single-phase and two-phase models at the same conditions at constant volume concentration of 2/3% and different values of Reynolds number while CuO nanofluid flows through microchannel with 6 pair of lvgs. As demonstrated in Figure 6, there is a good proportion between results of the used models at the considered conditions and the disagreement between results are less than 5 percent.

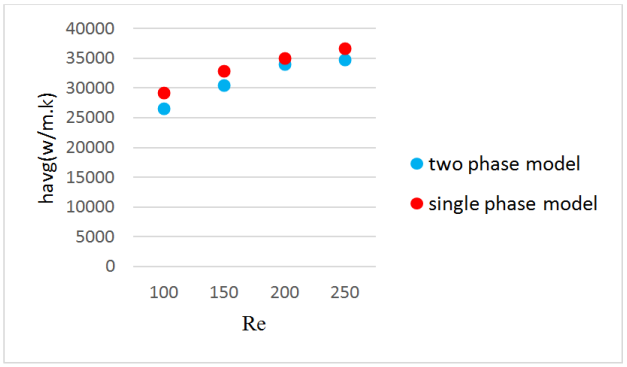

Figure 6. Comparison between two-phase and single-phase models

After comparison between these two models, the rest of simulations done under presented conditions and for single-phase model. Figs 7 describes the varieties of convective heat transfer coefficient against Rer for microchannel with different number of lvgs while pure water flows through microchannel as coolant. As expected using of vortex generators leads to higher heat transfer rates and this value increases by increasing the number of lvgs. Results indicate an improvement in the heat transfer coefficient of 22-35, 18-31 and 15-27 percent for microchannels with 6,4 and 2 pair of lvgs, respectively with variation of Re. small difference between heat transfer coefficient for plain microchannel and microchannel with lvgs at low Reynolds numbers is noticable, but this difference increases at higher Reynolds numbers.

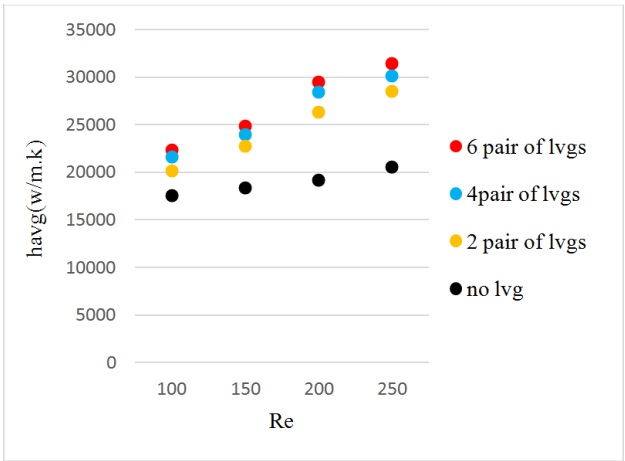

Figure 7. Variations of h_{avg} for different number of lvgs

To investigate the flow inside plain microchannel and lvg-enhanced microchannel more closely, figures 8 and 9 displays velocity and temperature contours inside both microchannels, respectively.

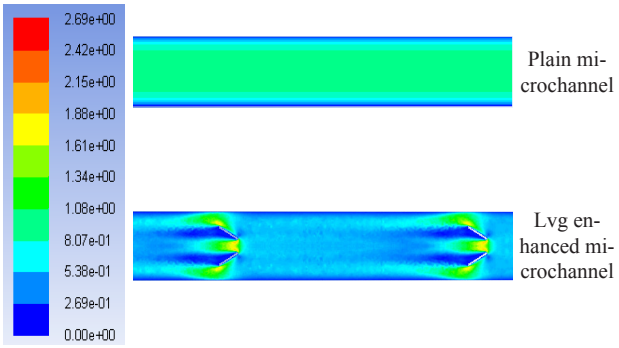

Figure 8. Velocity cantour for different channels

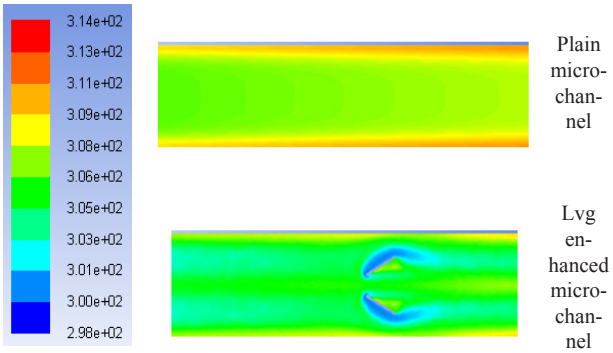

Figure 9. Temprature cantours for different channels

 DOI: https://doi.org/10.30564/jmer.v3i1.1568

Figures 10 and 11 represent the variation of convective heat transfer coefficient versus the plurality of Re for different volume concentrations inside microchannel with six pair of vortex generators and plain microchannel, while TiO_2 and CuO nanofluids flowing through, respectively. As was displayed in figure 7, Using lvgs increases the h_{avg} inside the microchannel, and as expected, using nanofluids instead of usual fluids such as water causes even greater heat transfer rates, also heat transfer rate rises with an increase in Re and volume concentration of nanoparticles. Using vortex generators inside microchannel creates vortices and wavy patterns back of lvgs, which this phenomenon leads to having even better mixed-flow, which causes greater heat transfer rates. Also, using nanofluids leads to greater heat transfer rates because of their better thermophysical properties, and higher Reynolds numbers reduce thermal boundary layer thickness behind lvgs and stronger and wider vortices, which also causes greater heat transfer rates. At fixed Re, it can be seen that with raising the volume concentration of nanoparticles, the effective thermal conductivity of fluid increases, which causes greater heat transfer rates because of higher thermal energy transfer because of the dispersion of fluid.

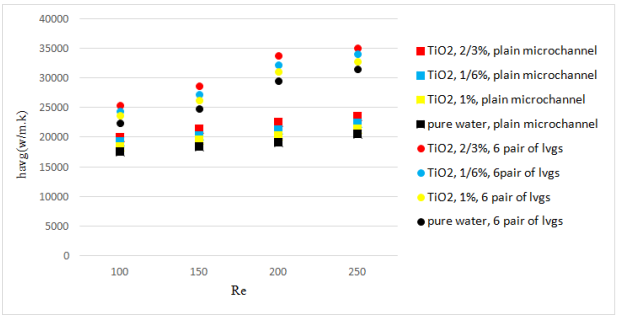

Figure 10. Variations of h_{avg} for diiferent volume concentrations of TiO2 nanofluid inside plain and lvg-enhanced microchannels

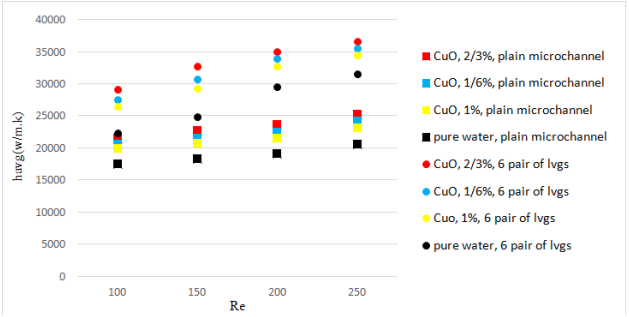

Figure 11. Variations of h_{avg} for diiferent volume concentrations of CuO nanofluid inside plain and lvg-enhanced microchannels

Results from flow of TiO_2 and CuO nanofluid inside plain microchannel and lvg-enhanced microchannel, showed enhancement in heat transfer performance of microchannel. As demonstrated in Figure 10 and 11, using TiO_2 nanofluid alone, increases heat transfer coefficient for about 4-12 percent which this value is about 9-18 percent for CuO nanofluid inside plain microchannel. Using both nanofluid and vortex generators causes even more increase in heat transfer coefficient, which is about 25-40 and 30-43 percent for TiO_2 and CuO nanofluids, respectively.

To compare the flow of three fluids used in this paper, figure 12 describes the varieties of convective h_{avg} for different Re for water and TiO2 and CuO nanofluids at a constant volume concentration of 2/3%. After Evaluating the results, it was found that the best performance happens when using CuO nanofluid as coolant flowing inside microchannel, either for lvg-enhanced or plain microchannel. Results demonstrates about 2-5 percent higher heat transfer coefficient when using CuO nanofluid compared to TiO_2 at different Reynolds number and volume concentrations.

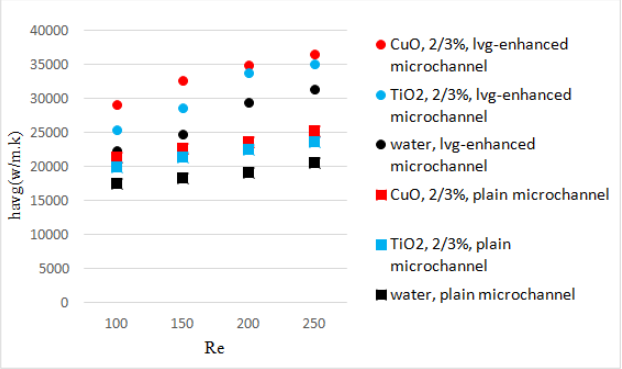

Figure 12. Comparison between results of two different nanofluids for plain and lvg-enhanced microchannels

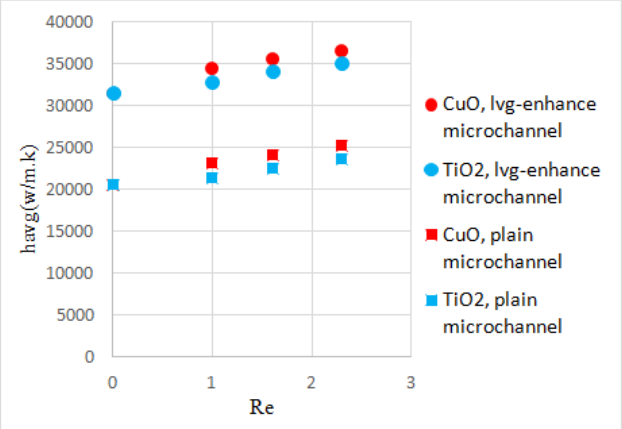

Figure 13. Variations of h_{avg} at constant Reynolds numbers for different volume concentrations

Figure 13 shows the variations of h_{avg} for different volume concentrations at Re=250, while TiO2 and CuO nanofluids flow through plain microchannel and

DOI: https://doi.org/10.30564/jmer.v3i1.1568

microchannel with six pairs of lvgs. As explained before, h_{avg} rises with an increase in nanoparticle volume concentration because of the increase of effective thermal conductivity of the fluid and higher thermal energy transfer. Figure 10 also shows better performance of CuO nanofluid compared to TiO2 nanofluid more obviously.

Another parameter that examined in this paper is the nusselt number. Figure 14 demonstrates varieties of Nu for different Re inside microchannels with a different number of vortex generators while water flows through as coolant. As was expected, Nu increases with an increase in Re and number of lvgs. The enhancement is about 12-30% for variations of Re and lvgs.

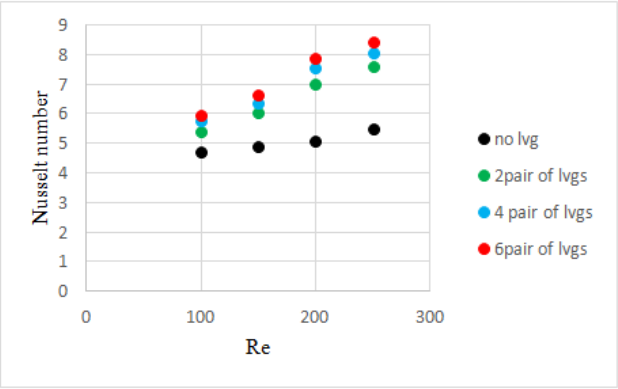

Figure 14. Variations of Nu for different number of lvgs

Figure 15 demonstrates variations of Nu versus different values of nanoparticle volume concentration for microchannel with six pairs of lvgs while TiO2 and CuO nanofluids flow through as coolant. Results show an increase in Nu by increasing the volume concentration of nanoparticles. The Nu increase is about 15% and 19% for TiO2 and CuO nanofluids, respectively.

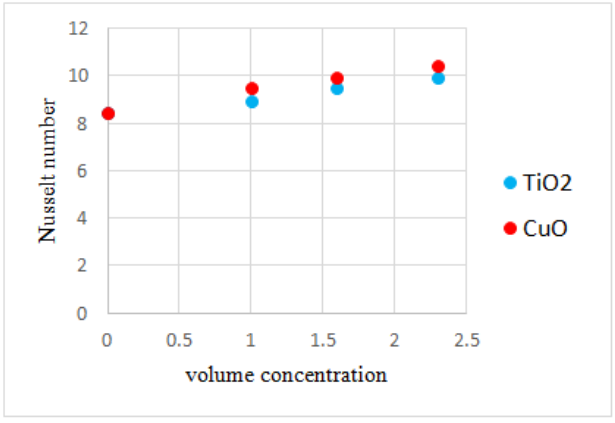

Figure 15. Variations of Nu at constant Re for different volume concentrations

One of the important parameters that should be investigated for flow inside microchannel, is pressure drop. Figure 16 shows the variations of pressure drop versus different nanoparticle volume concentrations inside lvg-enhanced microchannel at constant Reynolds number of 250 for TiO_2 and CuO nanofluids. As results show, by increasing the nanoparticle volume concentration, pressure drop inside microchannel increases for both nanofluids which is an adverse feature inside microchannel. This means using of nanofluids causes higher pressure drop inside microchannel, but due to small amount if increase in pressure drop than heat transfer rate enhancement, it can be neglected. Also results show that using vortex generators can also increase the pressure drop inside microchannel which can be neglected.

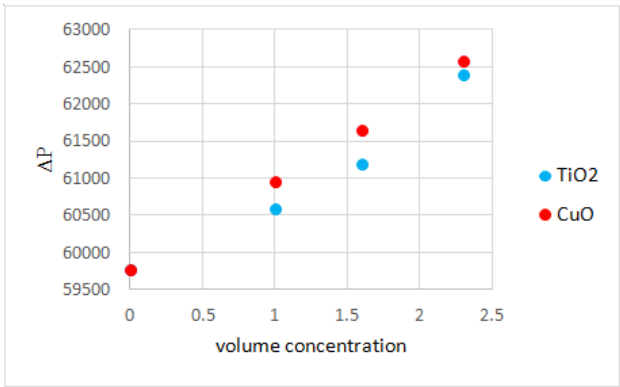

Figure 16. Variations of pressure drop for different volume concentrations

6. Conclusion

In this research, the flow and characteristics of two separate nanofluids inside a four-sided microchannel and the effects of using longitudinal vortex generators on the heat transfer performance of this microchannel investigated. A single-phase model employed to simulate nanofluids flow using ANSYS-FLUENT software. Summary of the findings of this study are as follows:

(1) Using nanofluids instead of common fluids like water, enhances heat transfer performance inside microchannel.

(2) Heat transfer coefficient increases by increasing the nanoparticle volume concentration and Re

(3) Using TiO2 and CuO nanofluids increased the heat transfer coefficient for about 4-12 and 9-18 percent for different volume concentrations, respectively.

(4) CuO nanofluids showed better performance inside microchannel than TiO2 nanofluid. The variation of the measured heat transfer coefficient was about 5%.

(5) Results showed that using vortex generators notably improves heat transfer rates inside the microchannel. It was found out that increasing the number of vortex gener-

 DOI: https://doi.org/10.30564/jmer.v3i1.1568

ators increases the heat transfer coefficient. This phenomenon can happen because of having a better-mixed flow, which causes greater heat transfer rates.

(6) Using vortex generators alone increases the heat transfer coefficient for about 15-35 percent for different number of lvgs. This value is about 25-45 percent when using nanofluids as a coolant inside microchannel.

(7) Using nanofluids and lvgs also causes an increase in pressure drop, which can be neglected.

7. Declarations

Authors' contributions

Arash Behaeen was in charge of the whole manuscript and wrote it. Mohammad Nimafar was the corresponding author and assisted with all the scientific issues and analysis.

Authors' Information:

Arash Behaeen, born in 1991 in Iran, received his master's degree in mechanical engineering from Central Tehran branch Islamic Azad University in 2017. His research interests include solar combi systems, fluid flow, and heat transfer of nanofluids and microchannels.

Mohammad Nimafar is currently an assistant professor of mechanical engineering at the central Tehran branch, Islamic Azad University Iran. He received his Ph.D. degree from Politecnico di Torino university in 2013. His research interests include numerical and experimental analyses of microstructures and nanofluid flow.

Competing Interests:

The authors claim that they have no competing concerns.

Funding:

Not applicable

Availability of Data and Material

Not applicable

Acknowledgments

Not applicable

References

[1] Toh, K., X. Chen, J. Chai. Numerical computation of fluid flow and heat transfer in microchannels. International Journal of Heat and Mass Transfer, 2002, 45(26): 5133-5141.

[2] Heris, S.Z., M.N. Esfahany, S.G. Etemad. Experimental investigation of convective heat transfer of Al2O3/water nanofluid in circular tube. International Journal of Heat and Fluid Flow, 2007, 28(2): 203-210.

[3] Bianco, V., et al.. Numerical investigation of nanofluids forced convection in circular tubes. Applied Thermal Engineering, 2009, 29(17-18): 3632-3642.

[4] He, Y., et al.. Numerical investigation into the convective heat transfer of TiO2 nanofluids flowing through a straight tube under the laminar flow conditions. Applied Thermal Engineering, 2009, 29(10): 1965-1972.

[5] Duangthongsuk, W., S. Wongwises. An experimental study on the heat transfer performance and pressure drop of TiO2-water nanofluids flowing under a turbulent flow regime. International Journal of Heat and Mass Transfer, 2010, 53(1-3): 334-344.

[6] Demir, H., et al.. Numerical investigation on the single phase forced convection heat transfer characteristics of TiO2 nanofluids in a double-tube counter flow heat exchanger. International Communications in Heat and Mass Transfer, 2011, 38(2): 218-228.

[7] Kalteh, M., et al.. Experimental and numerical investigation of nanofluid forced convection inside a wide microchannel heat sink. Applied Thermal Engineering, 2012, 36: 260-268.

[8] Lotfi, R., A.M. Rashidi, A. Amrollahi. Experimental study on the heat transfer enhancement of MWNT-water nanofluid in a shell and tube heat exchanger. International Communications in Heat and Mass Transfer, 2012, 39(1): 108-111.

[9] Fazeli, S.A., et al.. Experimental and numerical investigation of heat transfer in a miniature heat sink utilizing silica nanofluid. Superlattices and Microstructures, 2012, 51(2): 247-264.

[10] Nimafar, M., V. Viktorov, M. Martinelli. Experimental comparative mixing performance of passive micromixers with H-shaped sub-channels. Chemical engineering science, 2012, 76: 37-44.

[11] Nimafar, M., V. Viktorov, M. Martinelli. Experimental investigation of split and recombination micromixer in confront with basic T-and O-type micromixers. Int. J. Mech. Appl, 2012, 2(5): 61-69.

[12] Kabeel, A., T.A. El Maaty, Y. El Samadony. The effect of using nano-particles on corrugated plate heat exchanger performance. Applied Thermal Engineering, 2013, 52(1): 221-229.

[13] Shkarah, A.J., et al.. A 3D numerical study of heat transfer in a single-phase micro-channel heat sink using graphene, aluminum and silicon as substrates. International Communications in Heat and Mass Transfer, 2013, 48: 108-115.

[14] Viktorov, V., M. Nimafar. A novel generation of 3D SAR-based passive micromixer: efficient mixing and low pressure drop at a low Reynolds number. Journal of Micromechanics and Microengineering, 2013, 23(5): 055023.

[15] Aly, W.I.. Numerical study on turbulent heat transfer and pressure drop of nanofluid in coiled tube-in-tube heat exchangers. Energy Conversion and Management, 2014, 79: 304-316.

DOI: https://doi.org/10.30564/jmer.v3i1.1568

[16] Bianco, V., O. Manca, S. Nardini. Performance analysis of turbulent convection heat transfer of Al2O3 water-nanofluid in circular tubes at constant wall temperature. Energy, 2014, 77: 403-413.

[17] Zhang, J., et al.. Experimental study of TiO2–water nanofluid flow and heat transfer characteristics in a multiport minichannel flat tube. International Journal of Heat and Mass Transfer, 2014, 79: 628-638.

[18] Tiwari, A.K., et al.. Numerical investigation of heat transfer and fluid flow in plate heat exchanger using nanofluids. International Journal of Thermal Sciences, 2014, 85: 93-103.

[19] Sarafraz, M., F. Hormozi. Heat transfer, pressure drop and fouling studies of multi-walled carbon nanotube nano-fluids inside a plate heat exchanger. Experimental Thermal and Fluid Science, 2016, 72: 1-11.

[20] Arzani, H.K., et al.. Experimental and numerical investigation of thermophysical properties, heat transfer and pressure drop of covalent and noncovalent functionalized graphene nanoplatelet-based water nanofluids in an annular heat exchanger. International Communications in Heat and Mass Transfer, 2015, 68: 267-275.

[21] Xia, G., et al.. Numerical and experimental analyses of planar micromixer with gaps and baffles based on field synergy principle. International Communications in Heat and Mass Transfer, 2016, 71: 188-196.

[22] Sakanova, A., C.C. Keian, J. Zhao. Performance improvements of microchannel heat sink using wavy channel and nanofluids. International journal of heat and mass transfer, 2015, 89: 59-74.

[23] Behrangzade, A., M.M. Heyhat. The effect of using nano-silver dispersed water based nanofluid as a passive method for energy efficiency enhancement in a plate heat exchanger. Applied Thermal Engineering, 2016, 102: 311-317.

[24] Zarringhalam, M., A. Karimipour, D. Toghraie. Experimental study of the effect of solid volume fraction and Reynolds number on heat transfer coefficient and pressure drop of CuO–water nanofluid. Experimental Thermal and Fluid Science, 2016, 76: 342-351.

[25] Ebrahimnia-Bajestan, E., et al.. Experimental and numerical investigation of nanofluids heat transfer characteristics for application in solar heat exchangers. International Journal of Heat and Mass Transfer, 2016, 92: 1041-1052.

[26] Chen, X., et al.. Numerical and experimental investigation on micromixers with serpentine microchannels. International Journal of Heat and Mass Transfer, 2016, 98: 131-140.

[27] Sheikholeslami, M., et al.. CuOH2O nanofluid hydrothermal analysis in a complex shaped cavity. International Journal of Hydrogen Energy, 2016, 41(40): 17837-17845.

[28] Fsadni, A.M., et al.. Numerical study on turbulent heat transfer and pressure drop characteristics of a helically coiled hybrid rectangular-circular tube heat exchanger with Al2O3-water nanofluids. Applied Thermal Engineering, 2017, 114: 466-483.

[29] Zhang, J., et al.. An experimental investigation of heat transfer enhancement in minichannel: combination of nanofluid and micro fin structure techniques. Experimental Thermal and Fluid Science, 2017, 81: 21-32.

[30] Rao, M.S.E., et al.. Experimental investigation on forced convective heat transfer coefficient of a nano fluid. Materials Today: Proceedings, 2017, 4(8): 8717-8723.

[31] Diao, Y., et al.. Experimental investigation of MWCNT–water nanofluids flow and convective heat transfer characteristics in multiport minichannels with smooth/micro-fin surface. Powder Technology, 2017, 305: 206-216.

[32] Baheri, S., A. Alizad, R. Gharraei, Numerical Simulation of non-Newtonian Nanofluids Flow in Passive Injection Micromixers Using Mixture Model. Scientia Iranica, 2017, 24(1): 211-222.

[33] Sheikholeslami, M., M. Nimafar, D. Ganji. Nanofluid heat transfer between two pipes considering Brownian motion using AGM. Alexandria engineering journal, 2017, 56(2): 277-283.

[34] Sheikholeslami, M., M. Nimafar, D.D. Ganji. Analytical approach for the effect of melting heat transfer on nanofluid heat transfer. The European Physical Journal Plus, 2017, 132(9): 385.

[35] Fluent, A., 14.5 user's guide.. 2011: Fluent Inc., lebanon ,NH.

[36] Ranz, W., W.R. Marshall. Evaporation from drops. Chem. Eng. Prog, 1952, 48(3): 141-146.

 DOI: https://doi.org/10.30564/jmer.v3i1.1568

BILINGUAL PUBLISHING CO.
Pioneer of Global Academics Since 1984

Journal of Mechanical Engineering Research
http://ojs.bilpublishing.com/index.php/jmer

ARTICLE

An Experimental Study of Surface Improvement in FDM Parts by Vapor Treatment Process

Mayank Prajapati[1*] Sandeep Rimza[2]

Central Institute of Plastics Engineering & Technology: Institute of Plastics Technology (CIPET: IPT), Ahmedabad, Gujarat, 382445, India

ARTICLE INFO

Article history
Received: 1 February 2020
Accepted: 21 March 2020
Published Online: 31 March 2020

Keywords:
FDM
Vapor chemical process
Surface quality
Design of experiment

ABSTRACT

Fused deposition modeling is one of the most adaptable additive production method as a result of the value-effectiveness and environment-friendly nature. However, FDM technique nevertheless possesses primary problems in phrases of negative surface best due to including layer by using layer production method for the prototypes. It is acceptable to explore an efficient method for FDM elements to enhance the bad surface first-rate and dimensions precision. In the present research paper, an effort has been made to decorate the surface better and optimize the vital processing parameter of FDM based benchmark the use of vapor smoothing procedure (VSP). A comparative experimental take a look at has been completed by layout of experiments, Taguchi technique to analyse impact of input layout parameters at the floor finish of benchmark FDM parts. The outcomes of prevailing research display that VSP treatment improves the surface excellent of FDM components to micro stage with negligible dimensional variation. It is observed that improved floor excellent is observed in the 1,2, -Dichloroethane chemical at 90° component construct orientation, 0.25 mm layer thickness, 10% fill density and 90 sec Exposure times.

1. Introduction

Additive manufacturing (AM) process is gaining great importance and industrial demands to because of increase in complexity of product geometries. In this process conceptual model is made in a short span of time, economically with good characteristics [1]. The great spread of AM technologies has progressed as a fabrication method for fast tooling or rapid manufacturing products in low volume industrial applications [2]. Fused deposition modeling is one of the most widely used AM technologies. In the FDM technology, prototypes are built up by the data obtained from 3D CAD files and virtual model is converted into Standard Triangulation Language format [3]. The FDM also is known as 3-D printing layer-based manufacturing process, as extruding semi-solid thermoplastic materials solidifies in the form of thin slices on a fixtureless table [4]. The support material at the same time must be extruded, which acts as a support for the hanging fragments which can be detached later by manual cleaning or post-processing [5]. The use of AM technique for the different application is still possessed major difficulties in terms of poor surface finish. The poor surface finish limits the functionality of AM parts, and the reason

**Corresponding Author:*
Mayank Prajapati,
Central Institute of Plastics Engineering & Technology: Institute of Plastics Technology (CIPET: IPT), Ahmedabad, Gujarat, 382445, India;
Email: mayankcipet01@gmail.com

DOI: https://doi.org/10.30564/jmer.v3i1.1681

lies behind is the building strategy, layer thickness, orientation of the part, the geometry of enclosing surface, etc [6]. These drawbacks lead to dimensional inaccuracy and outweigh the advantages in FDM parts [7].

Many studies have been reported in the open literature to develop the quality of FDM parts since the origin of this technology. Galantucci et al. [8] investigated the FDM machining parameters on acrylonitrile butadiene styrene prototypes surface finish by chemical post-processing treatment has been investigated and yields a significant improvement of the Ra of the treated specimens. A dimensional accuracy of ABS specimens through post chemical treatment. It is naturally increases the surface finish and dimensional accuracy by Jayanth et al. [9]. J.S. Chohan et al. [10] revealed that, ABS specimens are manufactured by FDM and optimized vapor smoothing (VS) process for biomedical applications.Yifan Jin et al. [11] examine that chemical reaction mechanism during the treating process is analysed surface roughness for polylactic acid parts in FDM. R. Singh et al. [13] founded the surface finish of FDM based benchmarks through acetone exposure by using vapor smoothing station technique improving the surface finish nano-level with negligible dimensional deviations using a design of experiments technique. R. Singh et al. [14] inspect; surface hardness of ABS components has been improved through the HVS process by using acetone as smoothening media by scanning electron microscopic-based characterization of the components were carried out. Garg et al [15] search that, the simultaneous effect of part building orientation and raster angle on surface roughness, tensile strength, a flexural strength of ABS material. Lalehpour A. et al. [16] study the effect of the smoothing parameters on the resulting surface roughness of the final FDM products. The smoothing parameters are divided into the number of smoothing cycles and the cycle duration.

The use of FDM parts in different areas is till doubtful as the final part undergoes from rough geometrical roughness and a smaller amount geometrical tolerances in contrast to other AM technologies. However, various investigators have completed several experiment and investigation to evaluate the surface roughness and dimensional features of FDM parts by optimizing the input parameters.

The present study work, the authors is concentrated to improve the surface finish of FDM parts by using an alternative, cost effective volatile fluid (acetone, one-two-dichloroethane, butylalcohal). because it necessities marginal human intervention, the cost is very low and curing times are about few minutes. Taguchi L9 OA has been used to investigate the influence of factors such like as density of the parts, layer thickness, surface finish, build orientation and chemical exposure time for treated and untreated PLA samples.

Right now creators explore the connection between the FDM procedure parameters and the surface part of models, concentrating a strategy to improve the surface completion of the items. This technique performs better whenever contrasted with that revealed in refs. [16,17], in light of the fact that it needs minor human mediation, the expense is extremely low and relieving times are around a couple of moments minutes. Figure 1 shows the work process of the present paper. The trial action was done more than two stages, concentrating on autonomous factors in both the FDM procedure and the substance wrapping up. In the main stage, comprising of examples producing

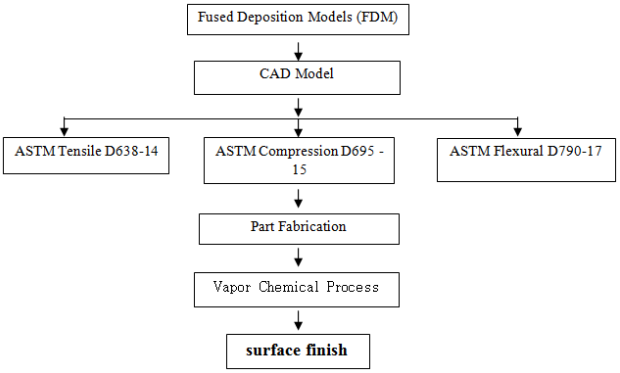

Figure 1. Experiment Strategy

2. Experimental Methodologies

Table 1. Experiment L9 orthogonal array for selected input factors at separate levels

Sr.no.	Layer thickness	Build orientation(°)	Density Fill (%)	Vapourization Time (sec)
1	0.20	0	10	90
2	0.20	90	50	120
3	0.20	90	100	150
4	0.25	90	10	90
5	0.25	90	50	120
6	0.25	0	100	150
7	0.30	90	10	90
8	0.30	0	50	120
9	0.30	90	100	150

To check out the have an impact on of layer thickness, the infill sample and infill percent, we used the Taguchi's L9 DOE. Taguchi's DOE was chosen as it adopts orthogonal arrays. This approach that each parameter has identical weights and may most fulfilling layout with the lowest range of Levels and minimum price. The L9 array calls for only nine Levels, however, for four parameter for 3 levels every, handiest the primary outcomes can be re-

 DOI: https://doi.org/10.30564/jmer.v3i1.1681

searched and no interactions, consequently, this paintings targets on the main effects. A four foremost parameters are selected for three level of each enter element through literature survey the experiments were designed by using Taguchi L9 orthogonal array in conjunction with independent variables. Table 1 reveals the experimentation elements and degrees.

2.1 Specimen Material

The scholarly CAD programming designer is utilized to make the models of the test examples ASTM D638-14, ASTM D695 - 15 and ASTM D790-17 are utilized for choosing the point by point measurements of malleable, pressure and flexural test examples separately. In the present work, all the examples are assembled utilizing PLA material is utilized to help structure age, while building the test examples. PLA material has the accompanying properties, rigidity = 57.8 MPa, elastic modulus = 3.3 GPa and flexural quality = 55.3MPa. A layer of help material at wanted areas is kept dependent on the art direction and geometric multifaceted nature. In the wake of building the part, the help materials are broken down in a help cleaning station. The models are spared in .stl position for cutting layer age and working of the examples. All examples are worked by saving a layer of 0.20, 0.25, 0.30 mm thickness.

2.2 Chemical Solvent

2.2.1 Acetone

The substantial and compound homes of $(CH_3)_2CO$ are given in Table 2. The substantial places of $(CH_3)_2CO$, alongside high dissipation rate, low thickness, and miscibility with water and various natural solvents make it appropriate to be utilized as a dissolvable. In view of its capability to experience expansion, oxidation/markdown, and buildup responses, CH3)2CO is utilized as a crude texture inside the synthetic blend of numerous business stock.

Table 2. Acetone properties

Molecular weight	Colour	Physical state	Melting Point	Boiling point	Solubility (water at 20°C)	Density-20°C,25°C,30°C	Solubility (organic solvent)
58.08	Colorless	Liquid	-95.35°C	56.2°C at 1 atm	Completely miscible	(0.78998g/ml, 0.78440g/ml, 0.78033g/ml)	Soluble in benzene and ethanol

2.2.2 1,2 Dichloroethane

1,2 dichloroethane is mostly used within the production of vinyl chloride as well as other chemical compounds. The properties of chemical shows in table 3. It is utilized in solvents in closed systems for various extraction and cleaning functions in natural synthesis. It is likewise delivered to leaded gas as a lead scavenger. It is also used as a dispersant in rubber and plastics, as a wetting and penetrating agent. It become formerly used in ore flotation, as a grain fumigant, as a steel degreaser, and in fabric and PVC cleaning.

Table 3 1,2 dichloroethane properties

Molecular weight	Colour	Physical State	Vapour pressure	water partition coefficient
98.96 g/mol	Colorless	heavy liquid that is slightly soluble in water	64 mm Hg at 20°C	1.48(log kow)

2.2.3 Butyl alcohol

1-Butanol is a type of alcohol with four carbon atoms being contained per molecule. Its molecular formula is $CH_3CH_2CH_2CH_2OH$ with three isomers, namely iso-butanol, sec-butanol and tert-butanol. It is colorless liquid with alcohol odor. A table 4 shows the properties detail.

Table 4. butyl alcohol properties

Melting point	Boiling point	Density	vapour density	Solubility
89 °C	117.6 °C	0.81 g/ml at 25 °C (lit.)	2.55 (vs. air)	water soluble

3. Results and Discussion

Surface roughness of FDM revealed PLA samples are measured earlier than and after chemical treatment with acetone, butyl alcohol and 1,2 dichloroethane. The components are fabricated at special element building orientations and their surface roughness, tensile; compression and flexural strength are measured. Measurements are completed for all components remedy and compared to have a look at and examine the impact of the exceptional parameters. Table 2, 3 and 4 indicates the results consequences of floor roughness values after chemical vaporization procedure on PLA specimens.

A story hardness is estimated utilizing a story unpleasantness analyzer (SJ 400) settling on a 0.25 mm cutoff length. Unpleasantness is estimated twice and the normal expense is mulled over and root folks rectangular hardness (Rq) values are estimated each nearby and over the length of the examples. Surface hardness of the segments are estimated close by and over the length of the examples multiple times on level floor and normal floor unpleasantness (Ra) and root recommend Rq values are thought about adaptations of Ra and Rq for each check tests developed at selective direction.

DOI: https://doi.org/10.30564/jmer.v3i1.1681

The whole manufactured parts are treated by uncovering the test examples to cold fume of $(CH_3)_2CO$, 1,2 dichloroethane and Butyl Alcohol. Because of $(CH_3)_2CO$, 1,2 dichloroethane and Butyl Alcohol harmfulness low or significant expense and worth dissipation pace of $(CH_3)_2CO$, 1,2 dichloroethane and Butyl Alcohol. In any case, the substance response with hot fumes or fluid CH3)2CO is resolved serious and every so often, it got hard to administer the harm of the part surfaces. To diminish harm brief presentation length is decided on warm fume. In any case, it is again found that every one surfaces are not managed consistently. Treatment by utilizing hanging of added substances would require appropriate equalization of $(CH_3)_2CO$, 1,2 dichloroethane and Butyl liquor worthy surface quality. In any case, the creators noticed that in treatment with hot fumes of $(CH_3)_2CO$, 1,2 dichloroethaneand Butyl Alcohol smoothen the part surface consistently. The holder is kept at a vaporization temperature for at vaporization time. Right now, improvement in surface completion and deviation experienced after fume handling were measured by subtracting the underlying and last qualities by utilizing the accompanying condition

$$= [(\text{Initial value} - \text{Final value})/\text{Initial value} \times 100] \quad (1)$$

Using Taguchi's layout For dimensional analysis, peak of the benchmarks changed into decided on judicially. Mintitab-17 software program package was used to find out the effect of processing of input parameters at the great traits of the patterns. Table No. 2 and no shows the stepped forward fee of surface finish of the patterns , dimensional deviation and their respective signal to noise (S/N) responses. Further ANOVA has been carried out for calculating the proportion contribution of input process parameters in surface roughness and dimensional deviation,

Figure 3 (a) and (b) shows the fundamental impact of S/N proportion on chosen process parameters for surface harshness and dimensional deviation separately. Further ANOVA has been directed for computing the rate commitment of info process parameters in surface hardness and dimensional deviation, appeared in table 2 Parametric reaction of S/N proportion for surface unpleasantness and dimensional deviation is given in table 2.

3.1 Discussion of Surface Roughness Effect of Butyl Alcohol Chemical Vapor

In this section represents the surface roughness improvement by butyl alcohol chemical vapor. The result of Surface roughness (SR) is shown in table 2 and figure 3(a) and figure 3(b) shows the minimum surface roughness is achieved at 0.25 mm layer thickness, 0° build orientation, 100% fill density and figure 4 (b) shows the minimum surface roughness is achieved at 0.25 mm layer thickness, 90° angle build orientation, 10% fill density and 90 sec time duration.

Table 2. surface roughness results With butyl alcohol

Sr. No	Layer Thickness(mm)	Build Orientation (°)	Fill density (%)	Time (Sec)	SR before chemical process (µm)	SR after chemical process (µm)
1	0.2	0	10	90	11.938	13.593
2	0.2	90	50	120	21.824	22.461
3	0.2	90	100	150	5.203	12.471
4	0.25	90	10	90	6.201	2.319
5	0.25	90	50	120	4.365	5.091
6	0.25	0	100	150	5.047	2.644
7	0.3	90	10	90	3.796	1.357
8	0.3	0	50	120	5.861	1.445
9	0.3	90	100	150	8.7963	2.225

Figure 2. ASTM D638-14 Tensile Specimen

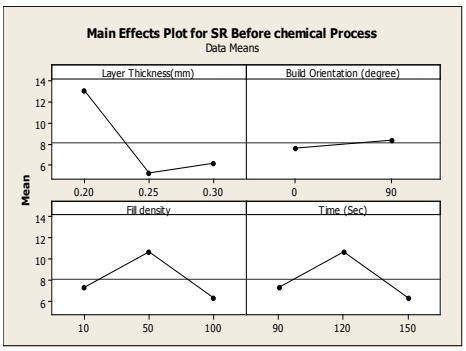

(a) Surface Roughness before chemical vaporization

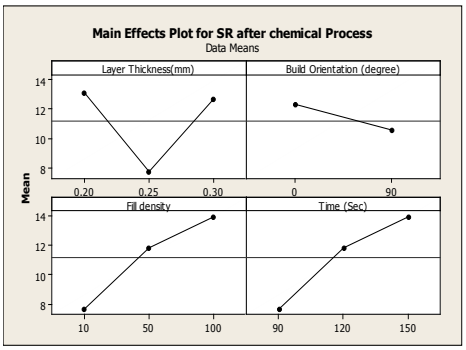

(b) Surface Roughness after chemical vaporization

 DOI: https://doi.org/10.30564/jmer.v3i1.1681

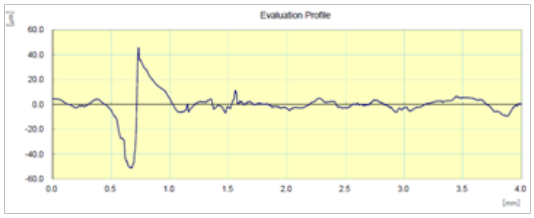

(c) Surface Roughness plot before chemical vaporization

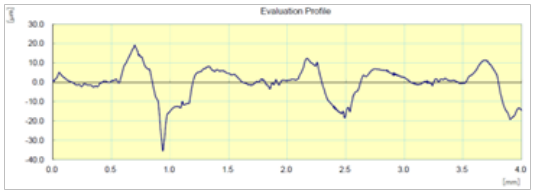

(d) Surface Roughness plot after chemical vaporization

Figure 3. Surface roughness result of Butanol or butyl alcohol

In figure 3 (a) shows the surface roughness is very rough at 0.20 mm thickness. This surface finish is very good at the 0.25mm and it is slightly rough at 0.30 mm thickness. The build orientation is not much effect on SR. where, fill density and chemical exposure time same affect on SR. It ia observes that, 100 % fill density and more chemical time exposure gives a good surface improvement this result is vice versa in figure 3 (b).

3.2 Surface Roughness Effect by Acetone Chemical Vapor

Surface roughness effect by acetone chemical vapor shown in table 3. A Figure 5 (a) observed that the minimum surface roughness is achieved at 0.30 mm layer thickness, 90° angle build orientation and 10% fill density Figure 5 (b) observed the minimum surface roughness is achieved at 0.30 mm layer thickness, 90° build orientation and 10% and 100% fill density and 90 and 150 sec time duration.

Table 3. surface roughness results with Acetone

Sr. No	Layer Thickness(mm)	Build Orientation (°)	Fill density %	Time (Sec)	SR after chemical process (µm)	SR after chemical process (µm)
10	0.2	0	10	90	13.593	6.710
11	0.2	90	50	120	22.461	19.604
12	0.2	90	100	150	12.471	12.865
13	0.25	90	10	90	2.319	3.521
14	0.25	90	50	120	5.091	2.718
15	0.25	0	100	150	2.644	16.986
16	0.3	90	10	90	1.357	12.826
17	0.3	0	50	120	1.445	13.209
18	0.3	90	100	150	2.225	11.958

Figure 4. ASTM D695 -15 Compression Specimen

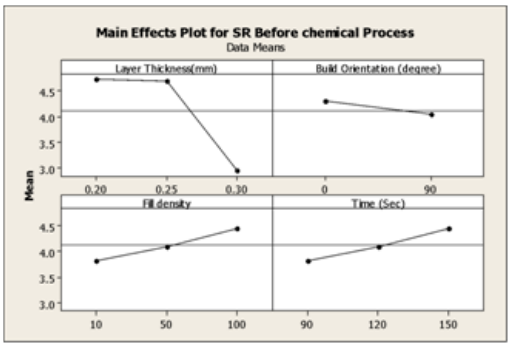

(a) Surface Roughness before chemical vaporization

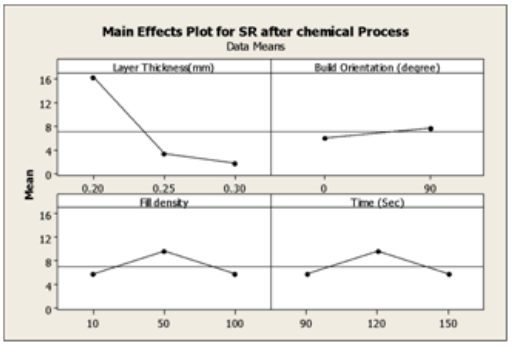

(b) Surface Roughness after chemical vaporization

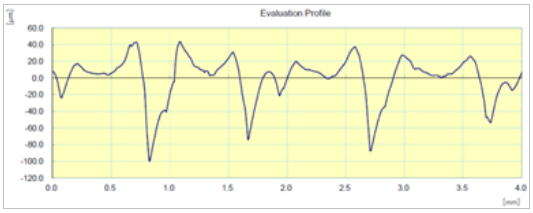

(c) Surface Roughness plot before chemical vaporization

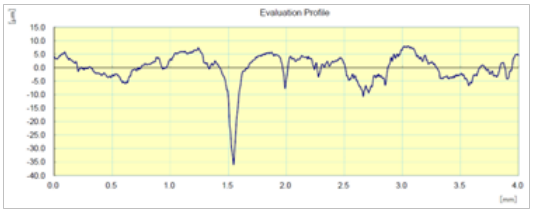

(d) Surface Roughness plot after chemical vaporization

Figure 5. Surface roughness result of Acetone

DOI: https://doi.org/10.30564/jmer.v3i1.1681

3.3 Discussion of Surface Roughness Effect by 1,2 Dichloroethane Chemical Vapor

Table 4 reveals the SR results of one-two dichloroethane. The minimum surface roughness is achieved at 0.20 mm layer thickness, 0° build orientation and 100% fill density in figure 7(a) and figure 7(b) observed the minimum surface roughness is achieved at 0.25mm layer thickness, 0° angle Build orientation, 100% fill density and 150 sec time duration.

Table 4. surface roughness results with 1,2 dichloroethane

Sr. No	Layer Thickness(mm)	Build Orientation (°)	Fill density (%)	Time (Sec)	SR Before chemical process (µm)	SR after chemical process (µm)
19	0.2	0	10	90	2.144	1.101
20	0.2	90	50	120	1.754	4.198
21	0.2	90	100	150	1.760	0.988
22	0.25	90	10	90	19.172	3.723
23	0.25	90	50	120	0.528	0.576
24	0.25	0	100	150	1.708	1.265
25	0.3	90	10	90	1.937	6.527
26	0.3	0	50	120	5.234	2.172
27	0.3	90	100	150	3.493	0.804

Figure 6. ASTM D790-17 Flextural Specimen

3.4 Discussion on Scanning Electron Microscopy (SEM) Analysis

SEM services are used to have a look at surface and particles, concentrated on failure analysis of the additives, visualization of texture and morphology, or contamination of cloth SEM analyses the surfaces of the materials, particles and fibers so that fine information can be measured and assessed via picture analysis. One of the important thing parameters of this look at evaluates the floor roughness of vapor polishing. Figure 8,9 and 10 compares the pinnacle sections on the surface roughness of 3-d printed part whilst determined the usage of SEM before and after the put up-processing. The microscopic image of the untreated PLA sample shown in Figure 8 (a), 9(a) and 10 (a). But from the microscopic images shown in Figure 8(b), 9(b) and 10(b), it is evident that the demarcation due to the 3D-printed raster disappears moderately due to the chemical treatment and the material in the top surface gets dissolved which fills the gap between the raster to form a uniform smoother outer surface, this is in accordance with the 2D roughness profile, i.e. as the immersion time increases, the surface roughness value decreases.

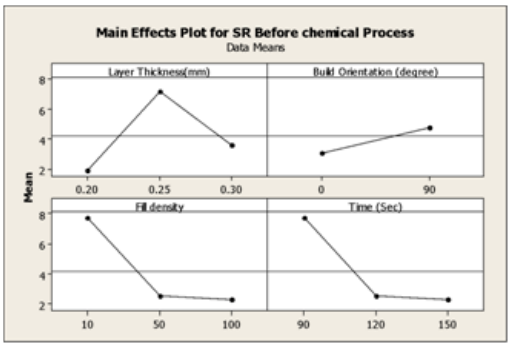

(a) Surface Roughness before chemical vaporization

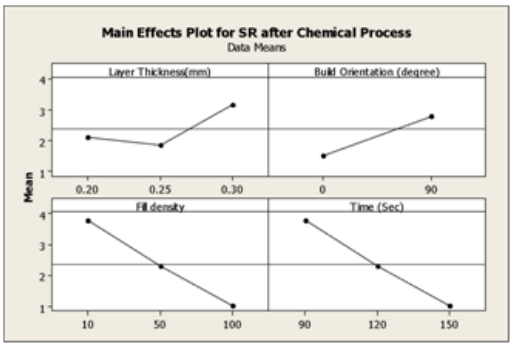

(b)Surface Roughness after chemical vaporization

(c) Surface Roughness plot before chemical vaporization

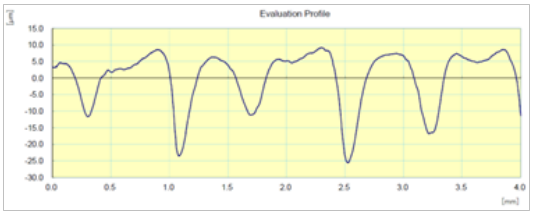

(d) Surface Roughness plot after chemical vaporization

Figure 7. Surface roughness result of 1, 2 dichloroethane

In all the instances the tensile electricity of acetone-dealt with samples is excessive than 1,2 dichloroethane treated samples but a lower floor roughness price is received via using 1,2 dichloroethane. This is due to the fact that PLA dissolves at a better fee in dichloroethane when in comparison to acetone and it makes the samples smoother and softer. From these consequences, a higher surface end is acquired using 1,2

DOI: https://doi.org/10.30564/jmer.v3i1.1681

dichloroethane. Hence, 1,2 dichloroethane may be used as an opportunity chemical to acetone for better surface finish improvement.

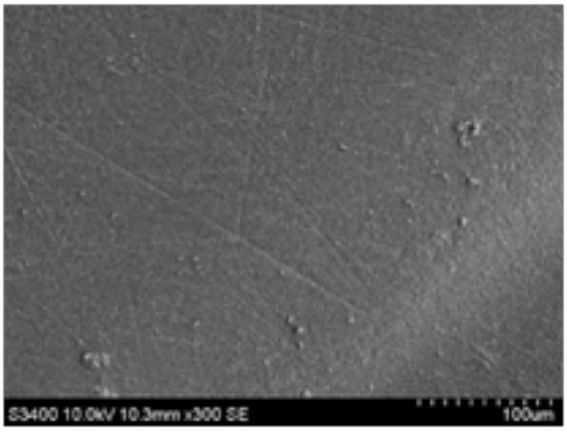

(a)

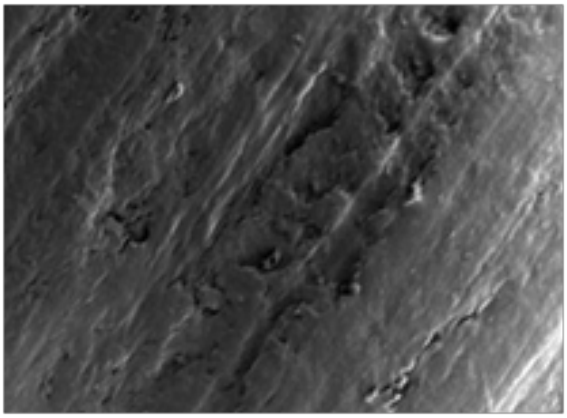

(b)

Figure 8. SEM images of ASTM D695-15 Tensile specimen butanol

Figure 8 (a) shows the line of deposited filament which were well arranged at the raster angle of 90º during printing. Whereas Figure 8 (b) illustrated the surfaces of the same surfaces after being exposed to cold vapor treatment. By comparing these figures, it shows that the cylindrical shape of the ABS filaments has dissolved by the chemical vapor to become a smooth surface after being exposed to the vaporization process.

Figure 8 show the ASTM D695-15 Standard specimen SEM images for improve the surface finish by chemical vapor process PLA parts with acetone chemical. It is observed that the minimum surface roughness is achieved at 0.30 mm layer thickness, 90° angle build orientation and 10% and 100% fill density and 90 and 150 sec time duration is achieved in part number 14.

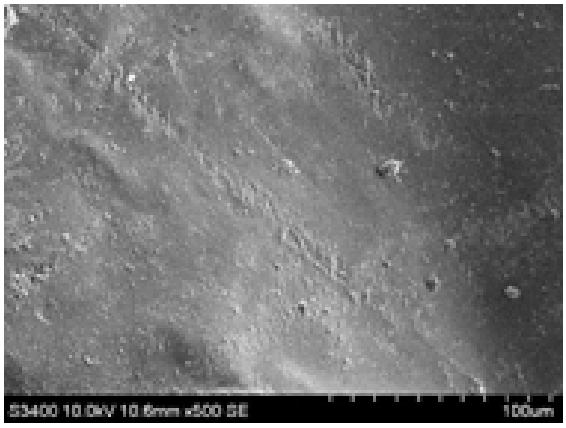

(a)

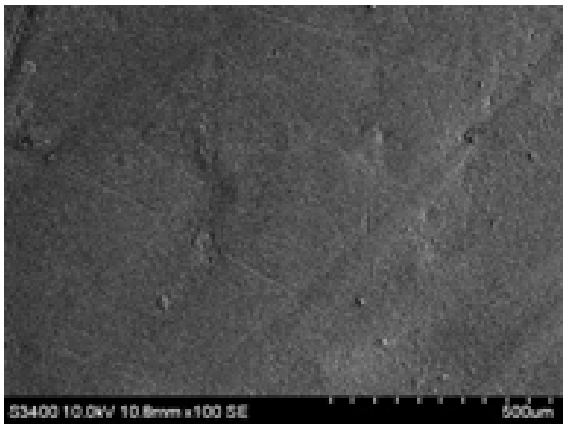

(b)

Figure 9. SEM images of ASTM D790-17 Flexural specimen with acetone

A flexural ASTM D790-17 Standard specimen SEM images shows in figure 9. It is improve the surface finish by chemical vapor process PLA parts with 1, 2 dichloroethane. The minimum surface roughness is achieved at 0.25mm layer thickness, 0° angle build orientation, 100%fill density and 150 sec time duration and it is good surface finish in part number 22.

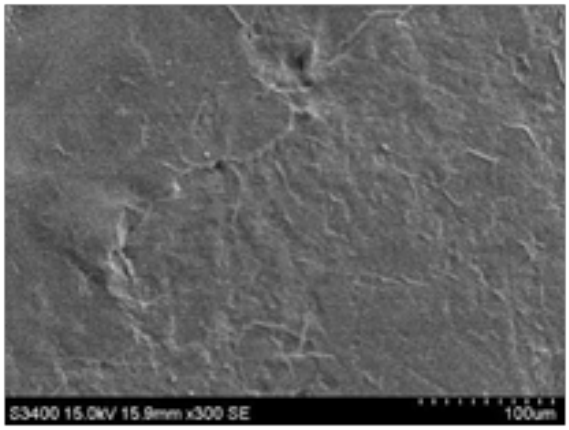

(a)

DOI: https://doi.org/10.30564/jmer.v3i1.1681

(b)

Figure 10. SEM images of ASTM D638-14 Compression specimen with 1, 2 dichloroethane

Figure 10 ASTM D638-14 Standard specimen for improve the surface finish by chemical vapor process PLA parts with butanol chemical. A minimum surface roughness is achieved at 0.25 mm layer thickness, 90° angle build orientation, 10% fill density and 90 sec time duration and good surface finish is achieved in part number 1.

4. Conclusion

In this present work, impact of component build, layer thickness, fill density and orientation. Surface roughness of FDM check specimens are investigated. The responses also are measured post constructed treatment by warm vapours of 1,2 dichloroethane, butanol acetone. The roughness of FDM printed elements is analysed process parameters have been shown to influence the Ra. Technique parameters have been shown to have an effect on the Ra. The surface roughness of FDM components constructed at two distinctive part orientations (0° and 90°) with chemical vapour treatment.It has been observed that the optimum surface finish is obtained at 90° part build orientation, 0.25 mm, layer thickness, 10% fill density and 90 second exposure time.

(1) The results are compared based on the results acquired and fractographic studies the following conclusions are:

(2) A butanol chemical vapour conditions of optimum parameters are 0° build orientation, 0.2 mm layer thickness, 10 % fill density and 90 second exposure time

(3) An acetone chemical vapour, the conditions of optimum surface finish are 90° build orientation, 0.25 mm layer thickness, 50 % fill density and 120 second exposure time.

(4) 1,2 dichloroethane chemical vapour experiment gives a rough surface, butanol gives little bit rough surface, while 1,2 dichloroethane gives a good surface finish improvement.

The optimum results of surface finish are 1,2 dichloroethane > butanol > acetone and optimum surface roughness is achieved by 1,2 dichloroethane.

Acknowledgement

The authors would like to thank the CIPET: IPT Ahmedabad for the grant to provide a facility in which to carry out this study.

References

[1] A. Mitchell, U.Lafont M. HołyńskaC.Semprimoschnig, Additive manufacturing - A review of 4D printing and future applications.

[2] N. Hopkinson, R. Hague, P. Dickens. Rapid Manufacturing An Industrial Revolution for the Digital Age, John Wiley & Sons, Chichester, West Sussex, 2005.

[3] A. Boschetto, V. Giordano, F. Veniali. International Journal of Advance Manufacturing Technology, 2012, 61: 945–956.

[4] T. Wholers, Wohlers report 2006: rapid prototyping & manufacturing state of the industry annual worldwide progress report, Wohlers Associates, Inc. Fort Collins, CO.

[5] Kruth JP, Leu MC, Nakagawa T. Progress in Additive Manufacturing and Rapid Prototyping. CIRP Annals - Manufacturing Technology, 1998, 47(2): 525–540.

[6] Kruth JP, Levy G, Klocke F, Childs THC. Consolidation Phenomena in Laser and Powder-Bed Based Layered Manufacturing. CIRP Annals – Manufacturing Technology, 2007, 56(2): 730–759.

[7] Gebhardt, A.. Understanding Additive Manufacturing. 2012, Carl Hanser Verlag.

[8] Daljinder Singh, Rupinder Singh, K.S. Boparai, Ilenia Farina, Luciano Feo, Anita, Kamra Verma. In-vitro studies of SS 316 L biomedical implants prepared by FDM, vapor smoothing and investment casting. Composites Part B, 2017.
DOI: 10.1016/j.compositesb.2017.08.019

[9] Siti Nur Humaira Mazlan, Mohd Rizal Alkahari1, Faiz Redza Ramli, Nurul Ain Maidin, MohdNizam Sudin, Ardzatul Ruziah Zolkaply. Surface Finish and Mechanical Properties of FDM Part After Blow Cold Vapor Treatment. Journal of Advanced Research in Fluid Mechanics and Thermal Sciences, 2018, 48(2): 148-155

[10] L.M. Galantucci, F. Lavecchia, G. Percoco. Experimental study aiming to enhance the surface finish of

fused deposition modeled parts. CIRP Annals - Manufacturing Technology, 2009, 58: 189–192.
DOI: 10.1016/j.cirp.2009.03.071

[11] J.S. Chohan, R. Singh, K.S. Boparai. Parametric optimization of fused deposition modeling and vapour smoothing processes for surface finishing of biomedical implant replicas. Measurement Journal, 2016, 94: 602-613.
DOI: https://dx.DOIl.org/10.1016/j,measurement.2016.09.001

[12] Yifan Jin, Yi Wan, Zhanqiang Liu. Surface polish of PLA parts in FDM using dichloromethane vapour. MATEC Web of Conferences 95, 05001 (2017) ICMME 2016.
DOI: 10.1051/matecconf/20179505001

[13] Rupinder Singh, Sunpreet Singh, Iqwinder Preet Singh, Francesco Fabbrocino, 2016. Investigation for surface finish improvement of FDM parts by vapor smoothing process. Composites Part B Engineering 111.
DOI: 10.1016/j.compositesb.2016.11.062

[14] Rupinder Singh, Sunpreet Singh, and Iqwinder P. Singh. Effect of Hot Vapor Smoothing Process on Surface Hardness of Fused Deposition Modeling Parts. 3D Printing and Additive Manufacturing 2016, 00(00).
DOI: 10.1108/RPJ-02-2014-0017

[15] Ashu Garg, Anirban Bhattacharya, Ajay Batish. Chemical vapor treatment of ABS parts built by FDM: Analysis of surface finish and mechanical strength. Int J Ady Manuf Technol.
DOI: 10.1007/s00170-016-9257-1

[16] N. Jayanth, P. Senthil & C. Prakash. Effect of chemical treatment on tensile strength and surface roughness of 3D-printed ABS using the FDM process, Virtual and Physical Prototyping, 2018.
DOI: 10.1080/17452759.2018.1449565

[17] Lalehpour, A., Janeteas, C. & Barari, A. Int J Adv Manuf Technol, 2018, 95: 1505.
https://DOI.org/10.1007/s00170-017-1165-5

[18] I. Gibson, D.W.R., B. Stucker. Additive ManufacturingTechnologies: Rapid Prototyping to Direct Digital Manufacturing. New York: Springer, 2010.

[19] Gurpal Singh Bual, Parlad kumar. Methods to Improve Surface Finish of Parts Produced by Fused Deposition Modeling" Manufacturing Science and Technology, 2014, 2(3): 51-55.
DOI: 10.13189/mst.2014.020301

DOI: https://doi.org/10.30564/jmer.v3i1.1681

BILINGUAL PUBLISHING CO.
Pioneer of Global Academics Since 1984

Journal of Mechanical Engineering Research
http://ojs.bilpublishing.com/index.php/jmer

ARTICLE

Development of Shape Memory Alloy Based Quarter Car Suspension System

P. Sathish Kumar[1*] R. Rajasekar[2] C. Sivasenapathy[2] Samir Kumar Pal[1]

1. Department of Mining Engineering, Indian Institute of Technology, Kharagpur, West Bengal - 721302, India
2. Department of Mechanical Engineering, Kongu Engineering College, Perundurai, Erode - 638060, India

ARTICLE INFO

Article history
Received: 25 February 2020
Accepted: 27 March 2020
Published Online: 31 March 2020

Keywords:
Shape memory alloy springs
Quarter car suspension
Harmonic profile

ABSTRACT

It is well-known that suspension systems plays a major role in automotive technology. Most of the today's vehicle applies a passive suspension systems consisting of a spring and damper. The design of automotive suspension have been a compromise between passenger comfort, suspension travel and road holding ability. This work aims in reducing the suspension travel alone by developing a quarter car model suspension for a passenger car to improve its performance by introducing shape memory alloy spring (Nitinol) instead of traditional spring. A two way shape memory alloy spring possesses two different stiffness in its two different phases (martensite and austenite). In this study, road profile is considered as a simple harmonic profile and vibration analysis of a miniature quarter car model suspension system has been carried out experimentally. Using theoretical method, the displacement of the sprung mass is also studied and discussed. The vibration analysis have been carried out for the suspension system at both phases of the spring and the results gives a significant improvement in reducing the displacement of sprung mass for various excitation frequencies.

1. Introduction

Suspension comprises the system of springs, shock absorbers and their linkages that connects vehicle to the wheels. Suspension system serves for the following purposes: contributing to the vehicle on-road holding/handling, braking in order to provide good active safety, driving pleasure, keeping passengers comfortable and well isolated from road noise, bumps, vibrations, etc. These above mentioned goals needs to be balanced, hence the design of suspension system involves adequate compromise [1-2]. A two-degree-of-freedom "quarter-car" automotive suspension system is shown in Figure 1. The suspension itself is shown to consist of a spring (Ks) and a damper (Ds). The sprung mass (Ms) represents the quarter car equivalent of the vehicle body mass. The unsprung mass (Mu) represents the equivalent mass due to the axle and tire. The vertical stiffness of the tire is represented by the spring (Kt). The variables Zs, Zu and Zr represent the vertical displacements from static equilibrium of the sprung mass, unsprung mass and the road respectively. Since it is difficult to perform analysis of a full car model, a single segment (quarter car model) has been studied [7].

**Corresponding Author:*
P. Sathish Kumar,
Department of Mining Engineering, Indian Institute of Technology, Kharagpur, West Bengal - 721302, India;
Email: sathishiitkgp@gmail.com

 DOI: https://doi.org/10.30564/jmer.v3i1.1716

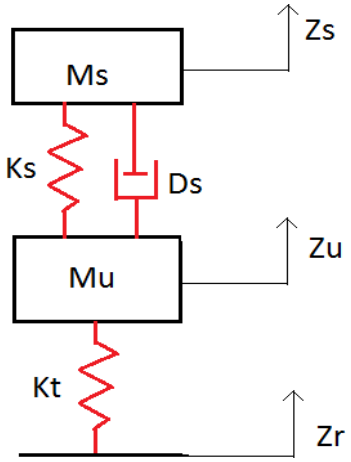

Figure 1. Quarter car suspension system

A shape memory alloy (SMA) is a material which remembers its original shape and when it is deformed within a limit, will return to its original shape when heated. This solid-to-solid phase transformation occurs when the material passes through a transformation temperature. If the transformation temperature is below 55oC, the material is in martensite phase and if it above 55oC, the material is in austenite phase [3-6]. Since heating an SMA spring causes change in elastic modulus of that material, a shape memory alloy spring possess two different stiffness at this two phases. Nitinol, nickel-titanium (Ni-Ti) alloys are the most important among all SMA's. These alloys typically are made of 55%-56% nickel and 44%-45% titanium [8-12].

The paper reports the vibrational effect of a miniature quarter car vehicle model when it is subjected to harmonic excitation by road profile. SMA spring is introduced into the suspension system and the amplitude of vibration is studied when the vehicle is moving with varying speeds on the harmonic profile.

2. Methods and Materials

Theoretical Analysis

The profile of the road is approximated to a line curve of amplitude 1.0 cm and a wavelength of 4.0 m. The sine wave is represented by q = Asinωt.

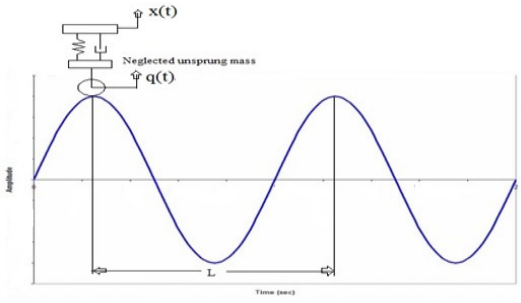

Figure 2. Harmonic road profile

q = road surface excitation in m.
A = amplitude = 0.01 m.
L= wavelength of road surface = 4 m.

Dimension and properties of Nitinol:

Spring outer diameter = 40 mm
Wire diameter = 6.5 mm
Number of coils = 12
Young's modulus of SMA spring at martensite (E_m) = 38 GPa
Young's modulus of SMA spring at austenite (E_A) = 80.95 GPa
Transformation temperature = 55°C
Stiffness at martensite (K_m) = 7230 N/m
Stiffness at austenite (K_A) = 15400 N/m

The natural frequency of the vehicle is given by

$\omega_n = \sqrt{(K/m)}$

m = sprung mass = 4.5 Kg,

Therefore, $\omega_{n1} = 40$ rad/sec, $\omega_{n2} = 58.50$ rad/sec

Damping constant of damper (C) = 300 Ns/m

Damping constant, $C = \xi 2m\omega_n$

Where, ξ = damping ratio. $\xi_1 = 0.83$ and $\xi_2 = 0.57$ are the damping ratio for the two different natural frequencies.

For the road profile mentioned and the velocity of the vehicle in Km/h, the excitation frequency is given by

$$\omega = V*(1/0.004)*(1/3600)*(2\pi) = 0.4363V \text{ rad/sec}$$

Where, V = velocity of vehicle in Km/h

The excitation frequencies (ω) were calculated for different car velocities and corresponding to these frequencies, amplitude of the response (X) is calculated by the equation

$$X = A\sqrt{\frac{1+(2\xi r)^2}{(1-r^2)^2+(2\xi r)^2}}$$

Where, r = (ω/ωn) = frequency ratio

The experimental set up consists of a test rig where an SMA spring and a damper is placed between an upper plate (sprung mass) and lower plate (unsprung mass). Both upper plate and lower plate are movable one which moves in a guide way. Figure 3 depicts the experimental set up. The excitation to the lower plate is given by cam rotation which is driven by a variable speed DC electric motor. The displacement of the upper plate due to cam rotation is measured by fixing an accelerometer at the upper plate, and measuring the signals with the help of DAQ card and DEWEsoft software.

DOI: https://doi.org/10.30564/jmer.v3i1.1716

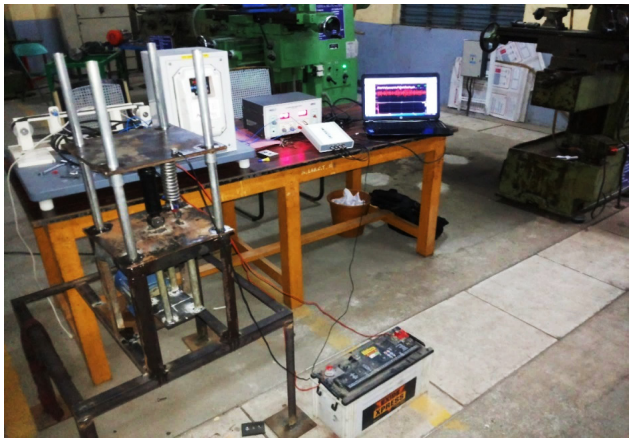

Figure 3. Experimental setup

3. Experimental Results and Discussion

Usually in a passenger car, the suspension system has the following parameters as unsprung mass = 45 kg, sprung mass = 320 kg, stiffness of spring = 45,000 N/m and damping constant of passive shock absorber = 3000 Ns/m. In the experimental setup, it is difficult to analyse the suspension system keeping the same sprung mass and unsprung mass. Also, the stiffness of the nitinol spring is not available upto 45,000 N/m. So, unsprung mass is taken as 4.5 kg and the commercially available SMA spring having stiffness in the range of 7230 N/m to 15400 N/m is taken for the experimental study.

The quarter car suspension system is operated with two natural frequencies because of the two spring stiffness of the SMA spring. When the spring is in its martensite phase (cold), (i.e., the system at its first natural frequency) the excitation is given to the lower plate through the cam and the response of the upper plate is measured using accelerometer in the quarter car setup. Further, when the spring transforms to austenite phase (hot), (i.e., the system at its second natural frequency) the same excitation frequency is given and the response of the upper plate is measured. The phase transformation of the spring from its cold phase to hot can be done by applying direct current to the spring from the battery.

The road profile taken in the theoretical analysis is reproduced by designing an eccentric cam and excitation to the system is applied through this latter.

Excitation frequency through cam (ω) = $2\pi N/60$

The different excitation frequencies taken in the theoretical method can be achieved in the experimental method by varying the speed of the motor which is connected to the cam. The amplitude responses for different excitation frequencies which are calculated theoretically and experimentally are tabulated as shown in table 1.

Table 1. Amplitude response values for different excitation frequencies

Vehicle speed (Km/h)	Speed of the motor (rpm)	Excitation frequency (Hz)	Amplitude X (m) at $\omega n1$		Amplitude X (m) at $\omega n2$	
			Theoretical	Experimental	Theoretical	Experimental
10	42	0.6944	0.010117	0.011121	0.010056	0.011034
20	83	1.3890	0.010438	0.011343	0.010221	0.011123
30	125	2.0832	0.010888	0.011811	0.010492	0.011523
40	167	2.7776	0.011366	0.012621	0.010862	0.011956
50	208	3.472	0.011771	0.013012	0.011317	0.012672
60	250	4.1664	0.012028	0.013632	0.011834	0.013452
70	292	4.8608	0.012100	0.013741	0.012381	0.014023
80	333	5.5551	0.011990	0.013573	0.012911	0.014256
90	375	6.2495	0.011730	0.013543	0.013367	0.014712
100	417	6.9439	0.011362	0.013122	0.013686	0.014802
110	458	7.6383	0.010927	0.012891	0.013820	0.015043
120	500	8.3327	0.010459	0.012543	0.013743	0.014846
130	542	9.0271	0.009984	0.011523	0.013466	0.014243
140	583	9.7215	0.009516	0.011231	0.013023	0.014067
150	625	10.4159	0.009067	0.010976	0.012467	0.013425

The graph for theoretical method is shown in figure 4.

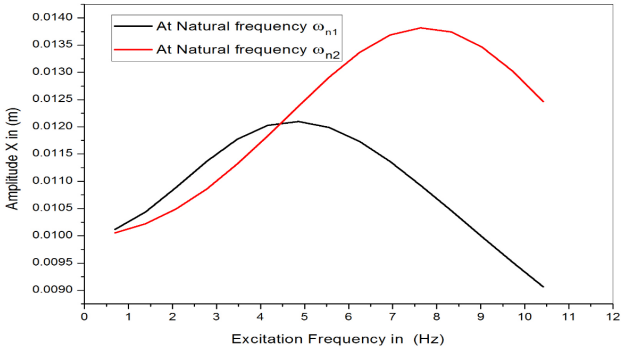

Figure 4. Theoretical sprung mass displacement for different excitation frequencies

The graph for the experimental method is shown in figure 5.

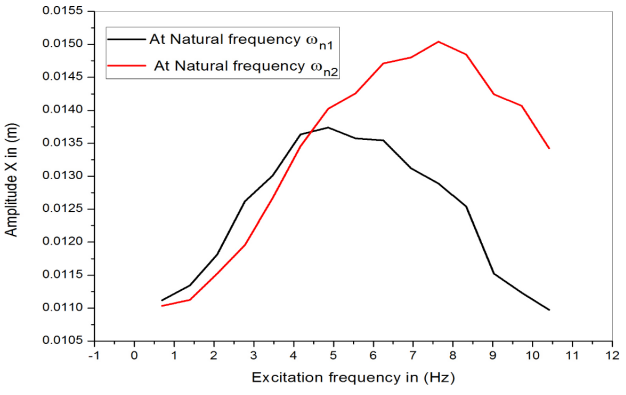

Figure 5. Experimental sprung mass displacement for different excitation frequencies

DOI: https://doi.org/10.30564/jmer.v3i1.1716

It is observed from the figure 4 that the amplitude increases upto an excitation frequency of 4.86 Hz and later drops for the suspension system operated with a natural frequency ω_{n1} (6.37 Hz). The maximum amplitude (0.012100 m) is achieved at excitation frequency of 4.86 Hz and this is due to the occurrence of resonance. The suspension system operating with natural frequency ω_{n2} (9.31 Hz) shows maximum amplitude of 0.013820 m at an excitation frequency of 7.63 Hz and later starts to decrease. This maximum amplitude is obtained because of resonance. The difference in maximum amplitude between the two natural frequencies is due to the fact that both are having different stiffness. It is noticed from the figure 4 that both the natural frequencies intersects at an excitation frequency of 4.5 Hz.

Figure 5 shows the experimental result of variation in amplitude. It is evident from figure 5 that the amplitude increases to an excitation frequency of 4.86 Hz and later it starts decreasing for the system (ω_{n1}). The maximum amplitude of 0.013741 m is attained at 4.86 Hz. Secondly for the natural frequency (ω_{n2}), the maximum amplitude of 0.015043 m is achieved at an excitation frequency of 7.63 Hz. The maximum amplitude achieved for both the natural frequencies are due to the existence of resonance and also it is clear that both the natural frequencies coincides at an excitation frequency of 4.5 Hz. Car suspension parameters considered for the analysis proves the attainment of constant excitation frequency of 4.5 Hz, when the vehicle moves at a speed of 65 Km/h.

4. Conclusion

Spring stiffness and damper rate are the two parameters which need to be controlled in designing a suspension system. Theoretical and experimental results conducted depicts difference in amplitude at the respective excitation frequencies, which may be due to non-linearity in the suspension parameters. It is clearly evident that upto an excitation frequency of 4.5 Hz, the amplitude is less for ω_{n2} system (9.31 Hz) and beyond excitation frequency of 4.5 Hz, the amplitude is less for ω_{n1} system at natural frequency of 6.37 Hz. Therefore, it is proposed that maintaining the natural frequency of 9.31 Hz until the car reaches 65 Km/h and retaining the natural frequency of 6.37 Hz beyond 65 Km/h will provide less vertical oscillations, when the vehicle is moving on the mentioned road profile. Further research will extend in reducing the reaction time of SMA spring during its transformation from martensite to austenite phase. Therefore, SMA springs with its property of variable stiffness can be best suited in the field of suspension systems in terms of vibration control applications.

References

[1] Sawant S.H, Mrunalinee V. Belwalkar, Manorama A. Kamble, Pushpa B. Khot, Dipali D. Patil. Vibration analysis of quarter car vehicle dynamic system subjected to harmonic excitation by road surface. International Journal of Instrumentation, Control and Automation, 2012, 1: 14-16.

[2] Chawan S.P, Sawant S.H, Tamboli J. A experimental verification of passive quarter car vehicle dynamic system subjected to harmonic road excitation with nonlinear parameters. IOSR Journal of Mechanical and Civil Engineering, 2278-1684: 39-45.

[3] Mirzaeifar R, Reginald D, Arash Y.. A combined analytical, numerical, and experimental study of shape-memory-alloy helical springs. International Journal of Solids and Structures, 2011, 48: 611-624.

[4] Switonski E, Mezyk A, Klein W.. Application of smart materials in vibration control applications. Journal of Achievements in Materials and Manufacturing Engineering, 2007, 24: 291-296.

[5] Zhang Y, Zhu S.. A shape memory alloy based reusable hysteretic damper for seismic hazard mitigation. Smart Materials and Structures, 2007, 16: 1603.

[6] Janke L, Czaderski C, Motavalli M, Ruth J.. Applications of shape memory alloys in civil engineering structures- overview, limits and new ideas. Materials and Structures, 2005, 38: 578-592.

[7] Zeinali M, Darus I.Z.M. Fuzzy PID controller simulation for a quarter car semi active suspension system using Magnetorheological damper. IEEE Conference on Control, Systems and Industrial Informatics, 2012, 978-1-4673-1023: 104-108.

[8] Tiseo B, Concilio A, Ameduri S, Gianvito A. A shape memory alloy based tuneable vibration absorber for vibration tonal control. Journal of Theoretical and Applied Mechanics, 2010, 48: 135-153.

[9] Liu X, Feng X, Shi Ye, Wang Ye, Shuai Z.. Development of a semi-activeelectromagnetic vibration absorber and its experimental study. Journal of Vibration and Acoustics, 2013, 135: 1-9.

[10] Attanasi G, Auricchio F, Urbano M. Theoretical and experimental investigation on SMA superelastic springs. Journal of Materials Engineering and Performance, 2010, 20: 706-711.

[11] Raczka W. Testing of a spring with controllable stiffness. Mechanics, 2006, 25: 79-86.

[12] Costanza G, Tata M.E, Calisti C. Nitinol one-way shape memory springs: thermomechanical characterization and actuator design. Sensors and Actuators A, 2010, 157: 113-117.

DOI: https://doi.org/10.30564/jmer.v3i1.1716

BILINGUAL PUBLISHING CO.
Pioneer of Global Academics Since 1984

Journal of Mechanical Engineering Research
http://ojs.bilpublishing.com/index.php/jmer

ARTICLE

Best Determined Position of Vents Based on Jet Cooling Model

Na Huang[1,2*] Yuhan Sun[1,3] Xiangjie Wu[1,4]

1. North China University of Technology Mathematical Modeling Innovation Lab, Tangshan, Hebei, 063210, China
2. School of Chemical Engineering, North China University of Technology, Tangshan, Hebei, 063210, China
3. School of Metallurgy and Energy, North China University of Technology, Tangshan, Hebei, 063210, China
4. School of mechanical engineering, North China University of Technology, Tangshan, Hebei, 063210, China

ARTICLE INFO

Article history
Received: 16 January 2020
Accepted: 17 January 2020
Published Online: 31 March 2020

Keywords:
Optimal Scheme
Jet Cooling Model
Fourier law
Thermal Conductivity

ABSTRACT

In some data centers, cold air is required to act on the cabinet to achieve cooling requirements, and the mixing of cold air and hot air reduces the utilization efficiency of cold air. In order to solve this problem, a jet cooling model is established to solve the optimal position of the outlet through the movement of cold air.

1. Introduction

The high-intensitive data processing of the data center is accompanied by a great quantity heat set free.For the sake of pledge the normal operation of the computer, the data center provides cold air in the open computer cabinet.Whereas,the combination of hot and cold air causes vast cold air to stay in the gap corridors and cracks of the cabinet, the utilization rate of cold air is very low, augment energy loss and resource squander.

2. Problem Analysis and Preparation

2.1 Dynamic Analysis of Cold Air and Cabinet System

In order to solve the problem that the temperature of the data center room lacks the data of airflow movement under the action of airflow, a central hypothermia cooling model is established to simulate the temperature change of the cabinet on the premise that the cold air directly acts on the cabinet and drives the hot air[1]. It reflects the direct utilization of cold air, As shown in

**Corresponding Author:*
Na Huang,
North China University of Technology Mathematical Modeling Innovation Lab, Tangshan, Hebei, 063210, China;
School of Chemical Engineering, North China University of Technology, Tangshan, Hebei, 063210, China;
Email: 1643360071@qq.com

 DOI: https://doi.org/10.30564/jmer.v3i1.1663

Figure 1.

*Analyze the now available size, shape and thermal power of the computer equipment in the data center cabinet, and determine the size of the cabinet type.

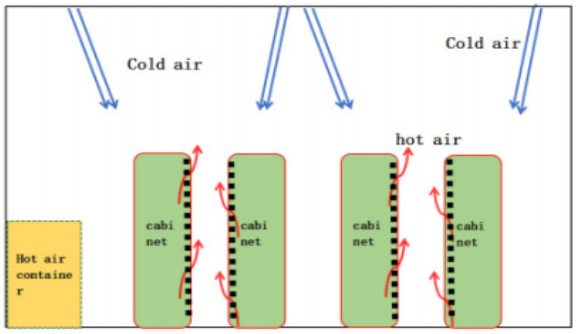

Figure 1. Schematic diagram of hot and cold air flow

2.2 Formulation of the Best Strategy

Four rows of cabinets are required as mentioned in the title.According to code for design of data center (GB 500174-2017), the specification of cabinet is 6000mm in and 600mm in width length. On the basis of different models, the cabinet is h = 42U, 36U and 24u, and ceiling height.

H= 3.2m, In order to maximize the use of cold air and reduce the loss of cold air, the direct contact between cold air and cabinet shall be increased as much as possible, and the cold air shall not be directly blown into the corridor or gap. Therefore, we set the position of the air outlet[2]. The ventilation angle requires the cold air to reach the top and bottom edge of the cabinet, so that the cold air drives the hot air flow and contacts the maximum area of the cabinet. For solving exact location the exit, the coordinate system is established with the length and width of the ceiling as the x-axis and y-axis. Then, on the basis of the geometric relationship of the room, we can calculated the position from the cabinet to the air outlet. This is the horizontal distance of the exit from the edge of the cabinet. The length of the room is determined by the distance between the four cabinets and the distance from the air outlet. To ensure that the maximum area of cold air acts on the cabinet, on basis of the actual situation, each branch pipe needs several outlets. In this way, the width of the room is determined, and the exact coordinates of the exit are finally given.

3. Establish Jet cooling Model

3.1 Hypothesis

(1) hypothesis leave out the effect of humidity of the air,water coolant,which on the internal system of air conditioning.

(2) assuming that the main computer is normal, that emit heat. And no fault heating.

(3) presume outdoor temperature doesn't affect indoor,that indoor temperature.

(4) suppose gas flow ,that the only effect factors is its own nature. have no connection with liquid level and solid wall.

3.2 Energy Analysis of Air and Cabinet

3.2.1 Conservation of Momentum of Cold Air

The cold air is entered into the motor room by means of the shower nozzle, diffusion in the motor room.Without the effect of liquid level and solid wall, free flow, forming free jet. Under this precondition, cold air knock against with ambient air, swop momentum, delivery some momentum to the swop air, and promote then to diffuse. It goes on and on, jet cross section is always increasing, the gaseous fluid moving around is escalation. So as to achieve the effect of hypothermia. Although, in the process, cold air loses its energy motion. Cold air and ambient air, the sun of momentum is a constant value. It can be represented by the following formula[3] .

$$q \times v = cons\tan t \qquad (1)$$

3.2.2 Regular of Velocity Decay

Free jet effect of cold air, and only it happened. In turn, change the blast of cold air. Focus on center speed, diminishing up and down boundary layer. Also, ambient air acquisition energy, enlargement flow rate, has been increasing. In case fix x-axis orientation, which direction of cold air expulsion. So under the premise of free jet, the blast of cold air is from center to both sides, little by little lessen. Among them, center blast attenuation has a pattern follow. As shown in figure 2.

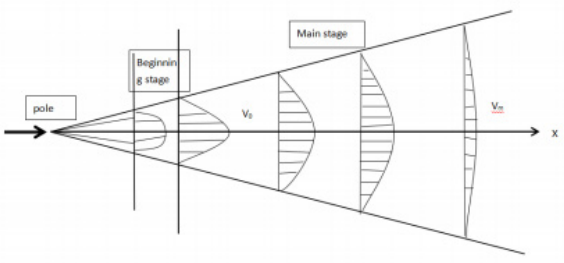

Figure 2. Free jet diagram

In the light of boundary layer theorem, law of conser-

DOI: https://doi.org/10.30564/jmer.v3i1.1663

vation, you can get, when free jet occurs, the pattern of cold air center blast. As shown in Figure 3 and formula (2).

$$v_m = \frac{0.96 v_0 r_0}{ay + 0.29 r_0} \tag{2}$$

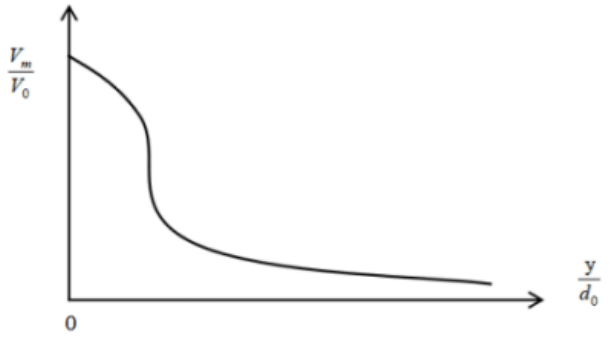

Figure 3. Diagram of center velocity curve of free jet

3.2.3 Air Solid Heat Conduction

The heat transfer between air and cabinet is convection heat transfer, and Fourier's law shows that all problems related to heat conduction can be solved by the following formula.

$$q = q_x j + q_y j + q_z k \tag{3}$$

According to Fourier's law and differential equation[4] of heat conduction, if the temperature of the medium around the object and the convective heat transfer coefficient between the object and the boundary are given, the expressions are as follows.

$$\lambda = \frac{-q \cdot \delta n}{\delta t \cdot n} = \frac{-a \Delta t \cdot an}{\delta t} \cdot K \tag{4}$$

That is, the temperature of the object medium and the surface thermal conductivity on the boundary surface are given, and the heat flux of convective heat transfer can be calculated.

3.3 The Foundation of Model

3.3.1 Model Basic Parameters

Basic parameters of the model: First, take ordinary cabinet as an example, which6.0m long, 0.6m wide, 42U high (1.867m). In data center, there are four rows of cabinets and air conditioning system. Combined with *Data Center Design Specification*, (GB 50174-2017). We are set to the length, width, and height of the room, L = 12.4m, W = 8.0m and H = 3.2m. At this point, distance between cabinet top and ceiling, H=1.333 meters, as shown in Figure 4.

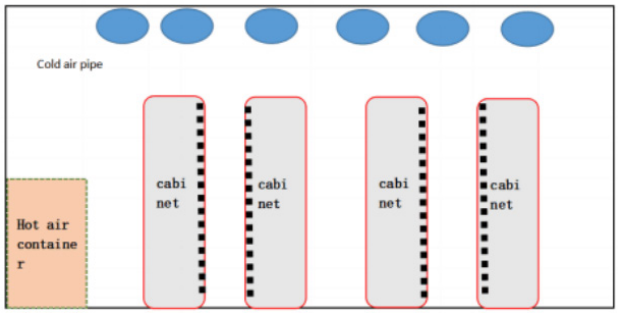

Figure 4. Plane elevation of cabinet room

3.3.2 Model Establishment

Model establishment: According to the flow law of jet, as shown in Figure 5, velocity of jet center in the initial section, equal to the initial speed, the velocity distribution curve of jet is changed. On the dimensionless coordinate system, draw velocity distribution curve. The empirical formula of central velocity is obtained[5] , that's formula (5).

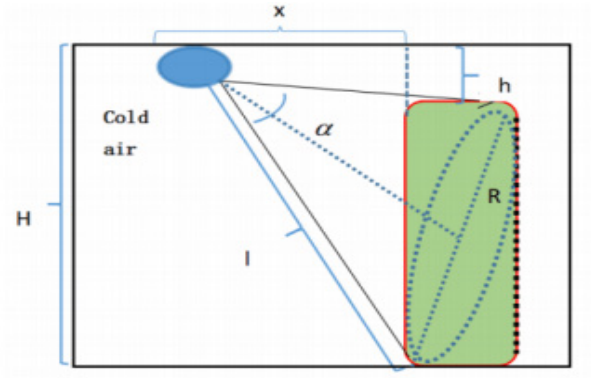

Figure 5. Diagram of the area of cold air acting on the cabinet (Mainview)

$$v = v_m [1 - (\frac{y}{R})^{\frac{3}{2}}]^2 \tag{5}$$

The injected fluid is spatially conical. As shown in Figure 5、6, when the cold air flow is brought into contact with the cabinet area when it is shot on the cabinet, the diagonal diagonal of the cabinet can be made to be the diameter of the jet cross section.

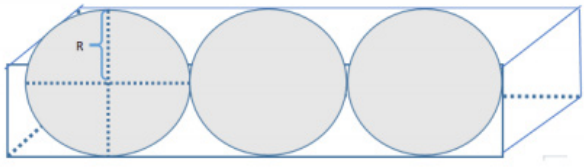

Figure 6. Diagram of the area of cold air acting on the cabinet (left view)

DOI: https://doi.org/10.30564/jmer.v3i1.1663

$$\begin{cases} v = v_m[1-(\frac{y}{R})^{\frac{3}{2}}]^2 \\ \lambda = \dfrac{-q\cdot\delta n}{\delta t\cdot n} = \dfrac{-a\Delta t\cdot an}{\delta t}\cdot K \\ v_{average} = \dfrac{(\int_0^y v_m[1-(\frac{y}{R})^{\frac{3}{2}}]^2\cdot 2\Pi y dy)}{\Pi R^2} \\ v_{average} = Kv_m = 0.257v_m \end{cases} \quad (6)$$

3.3.3 Conclusion

As can be seen from the above formula, When the speed v = 0, r = 1.9m, That is y=1.9m. It can be obtained by Fourier law and jet transfer formula. At the same time, According to the geometric relationship shown in (Figure 6), and the following four formulas, find out H = 1.333m, x = 2.333m.

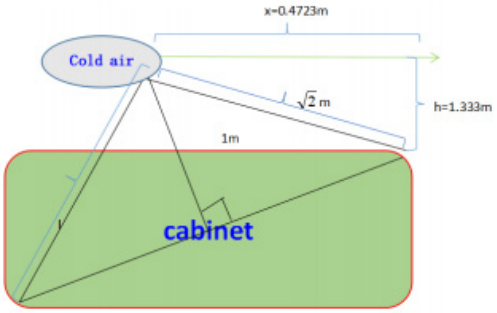

Figure 7. Schematic diagram of the relationship between x and h

As shown in figure 8, the length of the room is 8.4 m, because the cabinet is 6 m long, so to arrange a three exports, the cabinet to ensure sufficient to cool cabinet, can be designed as the width of the room is 8 m,(1.1277 m, 2 m) (1.1277 m, 4 m) (1.1277 m, 6 m), the same can be concluded that the coordinates of other nozzle respectively (3.0723 m, 2 m), (3.0723 m, 4 m) (3.0723 m, 6 m) (5.3277 m, 2 m) (5.3277 m, 4 m) (5.3277 m, 6 m) (7.2723 m, 2m) (7.2723m, 4m) (7.2723m, 6m).

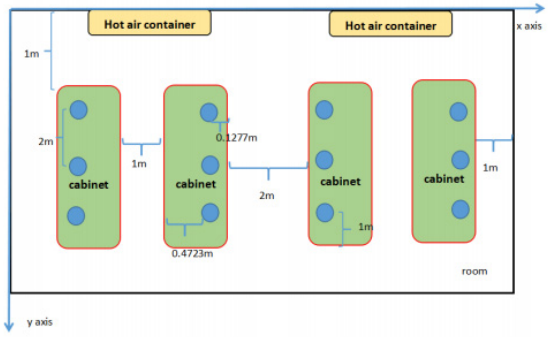

Figure 8. Large cabinet room layout top view

3.3.4 Analyze the Other Two Cabinet Types

The 36U cabinet(6m * 0.6m * 1.6m), is different in height, and the position of the exit should be re-established, taking v' = 0, then R' = 0.85m, then y' = 0.85m, h' = 1.6m > 1.3212m.Therefore, its best position is below the ceiling, and the length of the two edges of the airflow is taken. If the mixing degree of cold air and hot air increases, which reduces the utilization efficiency of cold air. If the contact area, between the cold[6].

$$\sum_{k=1}^{n} a_k^2 \sum_{k=1}^{n} b_k^2 \geq (\sum_{k=1}^{n} a_k b_k)^2$$

Deduced only at the time, established the equal sign, so can a bit of along to the ceiling, as shown in figure 9 the best position for export level, can be calculated according to the geometrical relationship, because in the process of solving large cabinets to determine[7] the room L = 8.4 m, W = 8 m, so not reality, so as shown in figure 10, set the leftmost export at the edge of the room, in the middle of the exports and the first type is the same. Then the export coordinates of the second model are respectively[8] (0, 2m) (0, 4m) (0, 6m) (3.0723m, 2m) (3.0723m, 4m)(3.0723m, 6m) (5.3277m, 2m) (5.3277m, 4m) (5.3277m, 2m) (8.4m, 2m) (8.4m, 4m) (8.4m, 6m).

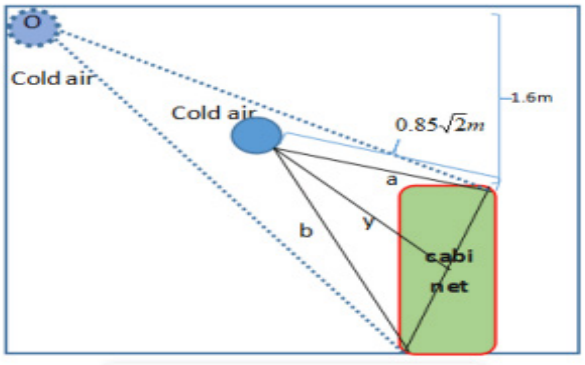

Figure 9. Schematic diagram of the area of cold air acting on a medium cabinet

Analyze the third kind of cabinet (6m * 0.6m * 1.068m), at this time, then, can be found, so the third kind of cabinet and the first kind of cabinet situation is the same, can be calculated according to the geometric relationship. Since the room size is D=1.7m, R=0.85m, the required coordinates should be the same as the design of the second cabinet outlet, the coordinates are respectively (0, 2m) (0, 4m)(0,6m) (3.0723m, 2m) (3.0723m, 4m) (3.0723m, 6m) (5.3277m, 2m) (5.3277m, 4m) (5.3277m, 6m)(8.4m, 2m) (8.4m, 4m) (8.4m, 6m).

DOI: https://doi.org/10.30564/jmer.v3i1.1663

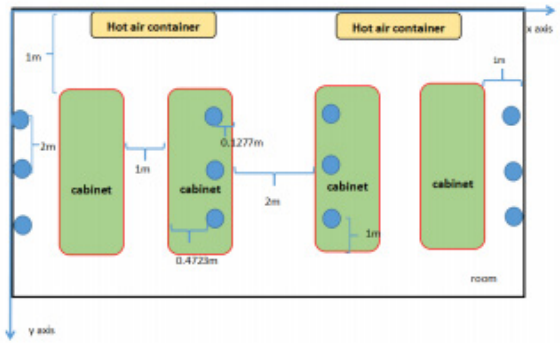

Figure 10. Top view of medium cabinet room layout

4. Conclusions

4.1 Distribution of Ventilation Outlet of Large Cabinet 42U

(1) The first column: (1.1277m, 2m) (1.1277m, 4m) (1.1277m, 6m)

(2) The second column: (3.0723m, 2m) (3.0723m, 4m) (3.0723m, 6m)

(3) The third column: (5.3277m, 2m) (5.3277m, 4m) (5.3277m, 6m)

(4) The fourth column: (7.2723m, 2m) (7.2723m, 4m) (7.2723m, 6m)

4.2 Distribution of 36U Ventilation Outlet of Medium Cabinet

(1) The first column: (0, 2m) (0, 4m) (0, 6m)

(2) The second column: (3.0723m, 2m) (3.0723m, 4m) (3.0723m, 6m)

(3) The third column: (5.3277m, 2m) (5.3277m, 4m) (5.3277m, 6m)

(4) The fourth column: (8.4m, 2m) (8.4m, 4m) (8.4m, 6m)

4.3 Small Cabinet 24U Ventilation Outlet Distribution

(1) The first column: (0, 2m) (0, 4m) (0, 6m)

(2) The second column: (3.0723m, 2m) (3.0723m, 4m) (3.0723m, 6m)

(3) The third column: (5.3277m, 2m) (5.3277m, 4m) (5.3277m, 6m)

(4) The fourth column: (8.4m, 2m) (8.4m, 4m) (8.4m, 6m)

References

[1] Yanhe Li, Runqing Zang, Qiuyu Zhang. Calculation of Heat Transfer Coefficient Prediction Model of Integrated Gravity Recirculation Cooler[J]. Thermal Science and Technology, 2019, 18(04): 272-277.

[2] JingJian Lu, Xun Zhang. Analysis of the impact of equipment plus pitch to the internal cabinet space laboratory flow and heat transfer[J]. Chinese Space Science and Technology, 2006(05): 53-59.

[3] Jiangke Zhao. "Water temperature air-conditioned room" using groundwater to exchange cold and heat[J]. Invention and Innovation (Comprehensive Edition), 2006(05): 42.

[4] Bingjie Zhang. Fluent-based research and simulation of indoor air-conditioning layout[J]. Straits Technology and Industry, 2019(01): 97-98 + 101.

[5] Weixiang Ding, Chunlin Liu, Hongmei Liu. Simulation study on the influence of different air supply parameters on indoor airflow organization and comfort based on orthogonal design[J]. Building Energy Efficiency, 2018, 46(11): 51-56.

[6] Rengang Yang, Dongdong Zhang, Feng He. Study on Transient Flow Field of Gas-Solid Two-Phase Free Jet[J]. Experimental Fluid Mechanics, 2005, 19(1).

[7] Yu Hu, Yingli Gong, Xinyu Sun, Xingliang Huang, Haiying Qi. Flow characteristics of free-spin jet with special structure[J/OL]. Journal of Tsinghua University (Science and Technology): 1-9 [2019-11-21].

[8] Qing Xie, Xiaoliang Guo, Junlong Xie, Zhiqiang Wang. Numerical simulation of free jet based on gas kinetics format[J]. Journal of Engineering Thermophysics, 2019, 40(07): 1498-1502.

 DOI: https://doi.org/10.30564/jmer.v3i1.1663

Author Guidelines

This document provides some guidelines to authors for submission in order to work towards a seamless submission process. While complete adherence to the following guidelines is not enforced, authors should note that following through with the guidelines will be helpful in expediting the copyediting and proofreading processes, and allow for improved readability during the review process.

Ⅰ. Format

- Program: Microsoft Word (preferred)
- Font: Times New Roman
- Size: 12
- Style: Normal
- Paragraph: Justified
- Required Documents

Ⅱ. Cover Letter

All articles should include a cover letter as a separate document.

The cover letter should include:

- Names and affiliation of author(s)

The corresponding author should be identified.

Eg. Department, University, Province/City/State, Postal Code, Country

- A brief description of the novelty and importance of the findings detailed in the paper

Declaration

v Conflict of Interest

Examples of conflicts of interest include (but are not limited to):

- Research grants
- Honoria
- Employment or consultation
- Project sponsors
- Author’s position on advisory boards or board of directors/management relationships
- Multiple affiliation
- Other financial relationships/support
- Informed Consent

This section confirms that written consent was obtained from all participants prior to the study.

- Ethical Approval

Eg. The paper received the ethical approval of XXX Ethics Committee.

- Trial Registration

Eg. Name of Trial Registry: Trial Registration Number

- Contributorship

The role(s) that each author undertook should be reflected in this section. This section affirms that each credited author has had a significant contribution to the article.

1. Main Manuscript

2. Reference List

3. Supplementary Data/Information

Supplementary figures, small tables, text etc.

As supplementary data/information is not copyedited/proofread, kindly ensure that the section is free from errors, and is presented clearly.

Ⅲ. Abstract

A general introduction to the research topic of the paper should be provided, along with a brief summary of its main results and implications. Kindly ensure the abstract is self-contained and remains readable to a wider audience. The abstract should also be kept to a maximum of 200 words.

Authors should also include 5-8 keywords after the abstract, separated by a semi-colon, avoiding the words already used in the title of the article.

Abstract and keywords should be reflected as font size 14.

Ⅳ. Title

The title should not exceed 50 words. Authors are encouraged to keep their titles succinct and relevant.

Titles should be reflected as font size 26, and in bold type.

Ⅳ. Section Headings

Section headings, sub-headings, and sub-subheadings should be differentiated by font size.

Section Headings: Font size 22, bold type

Sub-Headings: Font size 16, bold type

Sub-Subheadings: Font size 14, bold type

Main Manuscript Outline

Ⅴ. Introduction

The introduction should highlight the significance of the research conducted, in particular, in relation to current state of research in the field. A clear research objective should be conveyed within a single sentence.

Ⅵ. Methodology/Methods

In this section, the methods used to obtain the results in the paper should be clearly elucidated. This allows readers to be able to replicate the study in the future. Authors should ensure that any references made to other research or experiments should be clearly cited.

Ⅶ. Results

In this section, the results of experiments conducted should be detailed. The results should not be discussed at length in

this section. Alternatively, Results and Discussion can also be combined to a single section.

Ⅷ. Discussion

In this section, the results of the experiments conducted can be discussed in detail. Authors should discuss the direct and indirect implications of their findings, and also discuss if the results obtain reflect the current state of research in the field. Applications for the research should be discussed in this section. Suggestions for future research can also be discussed in this section.

Ⅸ. Conclusion

This section offers closure for the paper. An effective conclusion will need to sum up the principal findings of the papers, and its implications for further research.

Ⅹ. References

References should be included as a separate page from the main manuscript. For parts of the manuscript that have referenced a particular source, a superscript (ie. [x]) should be included next to the referenced text.

[x] refers to the allocated number of the source under the Reference List (eg. [1], [2], [3])

In the References section, the corresponding source should be referenced as:

[x] Author(s). Article Title [Publication Type]. Journal Name, Vol. No., Issue No.: Page numbers. (DOI number)

Ⅺ. Glossary of Publication Type

J = Journal/Magazine

M = Monograph/Book

C = (Article) Collection

D = Dissertation/Thesis

P = Patent

S = Standards

N = Newspapers

R = Reports

Kindly note that the order of appearance of the referenced source should follow its order of appearance in the main manuscript.

Graphs, Figures, Tables, and Equations

Graphs, figures and tables should be labelled closely below it and aligned to the center. Each data presentation type should be labelled as Graph, Figure, or Table, and its sequence should be in running order, separate from each other.

Equations should be aligned to the left, and numbered with in running order with its number in parenthesis (aligned right).

Ⅻ. Others

Conflicts of interest, acknowledgements, and publication ethics should also be declared in the final version of the manuscript. Instructions have been provided as its counterpart under Cover Letter.

About the Publisher

Bilingual Publishing Co. (BPC) is an international publisher of online, open access and scholarly peer-reviewed journals covering a wide range of academic disciplines including science, technology, medicine, engineering,education and social science. Reflecting the latest research from a broad sweep of subjects, our content is accessible worldwide – both in print and online.

BPC aims to provide an analytics as well as platform for information exchange and discussion that help organizations and professionals in advancing society for the betterment of mankind. BPC hopes to be indexed by well-known databases in order to expand its reach to the science community, and eventually grow to be a reputable publisher recognized by scholars and researchers around the world.

BPC adopts the Open Journal Systems, see on http://ojs.s-p.sg

Database Inclusion

Asia & Pacific Science Citation Index

Creative Commons

China National Knowledge Infrastructure

Google Scholar

Crossref

MyScienceWork

BILINGUAL
PUBLISHING CO.
Pioneer of Global Academics Since 1984

Tel:+65 65881289
E-mail:contact@bilpublishing.com
Website:www.bilpublishing.com

ISSN 2630-4945
01
9 772630 494207